

EVOLUTION OF THE INTRACLUSTER MEDIUM BETWEEN $0.2 < z < 1.3$ IN A *CHANDRA* SAMPLE OF 70 GALAXY CLUSTERS

TIMOTHY B. O'HARA,^{1,2} JOSEPH J. MOHR,^{1,2} & ALASTAIR J. R. SANDERSON³

Submitted to ApJ August 26, 2007

ABSTRACT

We study the evolution of the intracluster medium (ICM) with a uniformly analyzed sample of 70 galaxy clusters spanning $0.18 < z < 1.24$ and observed with *Chandra*. We find that X-ray luminosity and ICM mass at a fixed temperature evolve with redshift in a manner inconsistent with either the standard self-similar model of cluster formation or a model that assumes no evolution of cluster structure. Both luminosity and ICM mass evolve more slowly than the self-similar prediction, i.e., clusters have lower luminosity and ICM mass at fixed emission-weighted temperature than expected at higher redshifts. We find that evolution in these two observables can be modeled by a simple evolution in the cluster gas mass fraction, evolving as $(1+z)^{-0.39 \pm 0.13}$ when measured using core-subtracted observables. Excluding cluster cores from measurements results in evolution more consistent with the self-similar model than when the entire cluster is used, indicating that the fraction of clusters with cool cores increases with time, or that cool cores become more developed over time in those clusters that have them; this is supported by direct study of the redshift dependence of central surface brightness, which increases in scatter and magnitude at low redshift. We find that isophotal size-temperature relations evolve differently according to which isophote is used, indicating that the central and outer regions of cluster ICM evolve differently. We show that constraints on the evolution of the gas fraction and isophotal size-temperature relations constraints can be combined to measure cluster distances, and thus to constrain cosmological parameters in a way complementary to other techniques. Scatter in scaling relations is considerably reduced by using either core-subtracted quantities or three-parameter relations including the central surface brightness; in addition, there are indications that scatter decreases at higher redshift, suggesting that merging is not the dominant source of cluster structural variation. Our results provide constraints for simulations attempting to model cluster physics, indicate some difficulties for cosmological studies that assume constant cluster gas fractions, and point toward other potentially more robust uses of clusters for cosmological applications.

Subject headings: galaxies: clusters: general — X-rays: galaxies: clusters — intergalactic medium

1. INTRODUCTION

Scaling relations among bulk properties of galaxy clusters provide a powerful means to test models of the large-scale structure and evolution of the universe. These correlations among properties such as X-ray luminosity, intracluster medium (ICM) mass, mean ICM temperature, and cluster virial mass reflect gravitational and non-gravitational processes involved in the formation of structure in an expanding universe. Scaling relations also provide the means to readily estimate masses of clusters from much more easily measured properties such as luminosity, an essential component of cosmological studies that use X-ray observations to determine the redshift evolution of the cluster mass function.

Simple models of cluster formation via gravitational collapse predict particular forms for the redshift evolution of cluster scaling relations (Kaiser 1986). Adding additional cluster physics such as radiative cooling of the ICM, and energy injection by active galactic nuclei (AGN), supernovae, and star formation, modifies these predictions (e.g., Cavaliere et al. 1998; Ettori et al. 2004a; Muanwong et al. 2006; Kay et al. 2007). Observational

studies of scaling relation evolution are required to properly constrain models of cluster evolution and to understand the effects of non-gravitational processes on the scaling relations that will be used to study cosmology. X-ray studies of the ICM are complementary to studies of the evolution of the cluster galaxy population (e.g., de Propris et al. 1999; Lin et al. 2006), helping to constrain the overall evolution of cluster baryons and their distribution in various forms within clusters.

Several studies of X-ray scaling relation evolution have been carried out in recent years (e.g., Vikhlinin et al. 2002; Ettori et al. 2004b; Kotov & Vikhlinin 2005; Maughan et al. 2006; Morandi et al. 2007; Branchesi et al. 2007), but no clear consensus has emerged. In this paper we will address scaling relation evolution using a systematic analysis of a *Chandra* sample of 70 clusters covering $0.18 < z < 1.24$, the largest sample yet used for this purpose.

Our study addresses two difficulties which may affect scaling evolution measurements. The first arises from the fact that radiative cooling of the ICM leads to the development of cool, dense (and hence very luminous) cores in many clusters; these relatively small cores bias cluster measurements such as X-ray temperature and luminosity to an extent that they are not representative of the overall cluster structure. This introduces significant scatter into scaling relations; indeed, there is evidence that cool core clusters, which are traditionally regarded

¹ Department of Physics, University of Illinois, 1110 West Green St, Urbana, IL 61801; tbohara@astro.uiuc.edu, jmohr@uiuc.edu

² Department of Astronomy, University of Illinois, 1002 West Green St, Urbana, IL 61801

³ School of Physics and Astronomy, University of Birmingham, Edgbaston, Birmingham B15 2TT, UK

as “relaxed,” actually exhibit greater structural variation than non-cool core clusters, which are often thought to have recently undergone major mergers (O'Hara et al. 2006). Studies of scaling relations commonly attempt to “correct” for the impact of cool cores on cluster properties by one of several methods, such as simply leaving clusters with evidence for strong cool cores out of the sample (e.g., Arnaud & Evrard 1999), or excising central regions within a fixed metric radius (e.g., Morandi et al. 2007) or a fraction of the virial radius (e.g., Maughan et al. 2007), and perhaps “correcting” measured luminosity by some factor determined from a model of the cluster surface brightness distribution (e.g., Vikhlinin et al. 2002). In this paper we measure temperatures with and without cores defined as fractions of the virial radius, and we also measure luminosities with and without the same core. By using relations both with and without core subtracted quantities, we can examine the effects that core development has on cluster scaling relation slopes and evolution.

The other issue usually faced by scaling relation studies is the use of scaling relation slopes and normalizations from low-redshift studies carried out with different instruments. The relatively small fields of view of *Chandra* and *XMM-Newton* make measurements of local samples quite challenging with those instruments; hence, studies using older X-ray instruments are used as references for $z = 0$ relations. Unfortunately, differences in spectral and imaging results among X-ray instruments are well established, making such approaches subject to instrument-related systematics; indeed, even the same instrument has produced results differing by the author, as calibrations change and varying reduction and analysis methods are adopted. By using a large sample (70 clusters), we can avoid the use of outside references for scaling relation parameters or the direct inclusion of data from other samples, in favor of a single, homogeneously analyzed sample. While this approach is not entirely new—for example, Branchesi et al. (2007) studied evolution using their own 17 cluster sample both with and without the inclusion of data from other studies; and Morandi et al. (2007) studied a homogeneously reduced 24 cluster sample—the size of our sample leads to significantly smaller uncertainties on scaling relation parameters than have otherwise been obtained.

In § 2 we provide a brief overview of scaling relations and their predicted evolution, and in § 3 we explain our data reduction and measurement procedures. We test for scaling relation evolution with respect to expectations from the self-similar theory and from a scenario of no evolution in cluster parameters in §§ 4 and 5, respectively, and provide an explanation for observed evolution in scaling relations via a simple evolution in the gas mass fraction § 6. In § 7 we examine the evolution of isophotal size, and discuss the implications for studying cosmology using size measurements, and in § 8 we discuss the effectiveness of two different methods of reducing the scatter in measured scaling relations. In § 9 we compare our results to previous observations and simulation results, and discuss some implications of our findings. Finally, we list our conclusions in § 10.

We adopt the *WMAP* + LRG Λ CDM cosmology from Spergel et al. (2007), which combines the third year *WMAP* data with results from the SDSS luminous red

galaxy survey (Eisenstein et al. 2005) to give $H_0 = 70.9$ km s⁻¹ Mpc⁻¹, $\Omega_M = 0.266$, and $\Omega_\Lambda = 0.734$. All uncertainties are 68% confidence, unless specified otherwise.

2. SCALING RELATION BACKGROUND

The self-similar model (e.g., Kaiser 1986) describes formation of clusters via gravitational collapse of overdense regions in an expanding universe. In this model the ICM is heated by this gravitational collapse and the resulting shock heating, but no so-called non-gravitational heating is assumed. As a result, clusters scale self-similarly, i.e., they scale only because of changes in their physical size at fixed mass due to density variation as the universe expands. With the assumptions of spherical symmetry, hydrostatic equilibrium, a constant gas fraction, and X-ray emission dominated by thermal bremsstrahlung, this leads to X-ray luminosity L_X and ICM mass M_g scaling with ICM temperature T_X and redshift as

$$L_X \propto T_X^2 E(z), \quad (1)$$

$$M_g \propto T_X^{3/2} E(z)^{-1}, \quad (2)$$

where $E(z)$ is the ratio of the Hubble parameter at redshift z to its present value. In a flat cosmology with matter density Ω_m , $E(z)$ has the form:

$$E(z) = H(z)/H_0 = [\Omega_m(1+z)^3 + 1 - \Omega_m]^{1/2}. \quad (3)$$

Predicting scaling laws for the isophotal size (i.e., the physical size of the region corresponding to the angular size of a particular X-ray isophote; see § 3.5) requires additional assumptions about the ICM mass distribution. If the ICM distribution scaled self-similarly with mass, then isophotal size scales as

$$R_I \propto T_X^{2/3}, \quad (4)$$

with no redshift evolution if the ICM density falls off as r^{-2} outside the core (i.e., $\beta = \frac{2}{3}$; Mohr et al. 2000).

Observational studies have found that scaling relations for all three of these observables (L_X , M_g , and R_I) in fact have a stronger dependence on temperature than predicted by self-similar models (e.g., Edge & Stewart 1991; Markevitch 1998; Mohr & Evrard 1997; Mohr et al. 1999). Explanations for this and other evidence of non-gravitational processes, such as the presence of entropy ramps in the central regions of clusters (e.g., Ponman et al. 2003), typically involve additional energy injection by active galactic nuclei (AGN), supernovae, and star formation (e.g., Bialek et al. 2001; Bower et al. 2001; Borgani et al. 2002; McCarthy et al. 2004; Kay et al. 2007); radiative cooling of the ICM, which leads to the formation of cool, dense cores in many clusters; and non-radiative cooling (e.g., Bryan 2000).

It is important to note that there are multiple ways to define radii for measuring cluster parameters, which result in different predicted redshift evolution for scaling relations. The expressions given above are correct for observables (L_X and M_g) measured within regions corresponding to fixed overdensities relative to the critical density. This is appropriate for our strategy in this paper, in which we choose to measure cluster properties within virial regions defined by local relations, and

then test for consistency with the evolution scenarios described below. Another commonly used form for the redshift evolution of scaling relations (e.g., Ettori et al. 2004b; Branchesi et al. 2007; Morandi et al. 2007) uses densities defined from assumptions of virial equilibrium in a spherical collapse model. These densities have their own redshift evolution, leading to additional factors in the scaling relation evolution equations. In either case, it is common to parametrize additional redshift evolution beyond the self-similar predictions in terms of a simple power law with redshift, i.e., proportional to $(1+z)$ raised to some power.

In this paper we discuss two models for cluster evolution. The first is “self-similar evolution,” in which cluster observables scale as would be expected given purely gravitational influence as discussed above, i.e., $L_X \propto E(z)$ and $M_g \propto E(z)^{-1}$. The other is what we will refer to as “no evolution,” meaning that cluster parameters, including virial radii, do not scale at all as the universe expands.

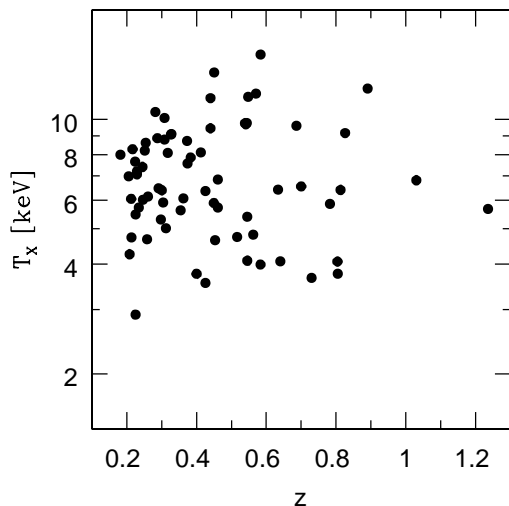


FIG. 1.— Measured emission-weighted mean temperature T_X plotted versus redshift for the clusters in our sample.

3. DATA REDUCTION

3.1. The Cluster Sample

The data are drawn from the *Chandra* archive. The lower redshift limit of $z \sim 0.2$ reflects the difficulty in measuring cluster parameters out to at least r_{2500} for clusters closer than this, given the small *Chandra* field of view. The cluster sample is listed in Table 6, with the ID number of the *Chandra* observation used for each cluster.

Having been largely developed through cluster selection in archival *Einstein* IPC and *ROSAT* PSPC observations, our sample is essentially X-ray flux limited. However, as the sample is not derived from a single homogeneous survey at a fixed flux threshold, it might be expected to include systematically more luminous (i.e., more massive) systems at high redshifts. In Figure 1 we plot the emission-weighted mean temperatures for our sample (measured as described in §3.3 below) versus redshift. Our sample spans a consistent range of T_X over the full redshift range.

3.2. X-ray Data Reduction

The data reduction is carried out using the standard *Chandra* analysis software CIAO, version 3.3, with CALDB version 3.2.1, and the spectral fitting package XSPEC, version 11.3.1. We generate new level 2 events files from the level 1 files obtained from the *Chandra* archive, so that all observations are reduced in a uniform manner. The following reduction procedure is applied to each cluster.

Light curves are extracted for back-illuminated chips 5 and 7 individually, and for front-illuminated chips 0–3 and 6 combined. Light curves are extracted and binned in time using the recommended criteria for each chip.⁴ Flares are excluded using the CIAO task “LC_CLEAN” based on the median value of the light curve. The exposure times after filtering are given in Table 6.

Cosmic ray events are identified with the CIAO tool “ACIS_RUN_HOTPIX”. A new level 1 events file is then generated using the latest gain file, and charge transfer inefficiency (CTI) and time-dependent gain variation corrections are applied as appropriate. Standard bad columns and hot pixels are excluded. Events with ASCA grades of 0, 2, 3, 4, and 6 are used. A level 2 events file is then created from the filtered level 1 events file. Where the observation was made in very faint (VF) mode, we carry out the extra background event flagging that this enables.

We attempt to use background data from the actual data sets, extracting the background from regions well away from target cluster or other emission. For some clusters, however, emission fills most of the detector, and in these cases we extract the background spectrum from the Markevitch blank-sky data.⁵ To account for small differences in the particle background between these statistical backgrounds and each individual observation, the blank-sky sets’ exposure times are scaled by the ratio of counts in the 7–12 keV energy band in the data and blank-sky observations. Before using either background method point sources are identified by the iterative method described in Sanderson et al. (2005) and checked by visual inspection, and then excluded. Even when emission-free regions are available, if the spectral fit is worse with the local background than with the blank-sky background, we use the latter. In total, we use the blank-sky backgrounds for 41 of the 70 clusters in our sample.

3.3. Spectral Fitting

Cluster spectra are extracted in regions with maximum radius chosen by eye to be where the cluster emission merges into the background; the center coordinates and radii of our extraction regions are given in Table 6. Choosing apertures based on the X-ray surface brightness distribution might result in smaller apertures relative to the physical size of clusters that are cooler or lie at higher redshifts, and thus will tend to have observations with fewer total counts. However, Figure 2, which plots the ratio of the spectral extraction radius to r_{500} for each cluster versus cluster mean temperature (*left*) and redshift (*right*), suggests that this is not the case. The mean ratio of aperture radius to r_{500} is 0.84 ± 0.20 (RMS), with no apparent temperature or redshift dependence.

⁴ <http://cxc.harvard.edu/ciao/>

⁵ <http://cxc.harvard.edu/contrib/maxim/acisbg/>

We generate weighted response matrix files (RMFs) using the CIAO tool MKACISRMF when the data allow; otherwise we use the older tool MKRMF.

We fit to the cluster spectra a single-temperature APEC model with a component for galactic absorption. We use fit N_{H} values when they are reasonable (i.e., within a few standard deviations of the galactic value), and not pegged to zero; otherwise, we fix N_{H} to the galactic value (Dickey & Lockman 1990). In total, we fit N_{H} for 18 of the 70 clusters. We generally extract spectra in energy bands of 0.7–9 keV for ACIS-I, and 0.5–9 keV for ACIS-S. In a few cases we use an upper limit of 7 keV when there is clearly spurious, non-background emission above this value; in no case does this change the measured temperature at greater than the 1–2% level. We use the Cash statistic (Cash 1979), which is preferable to χ^2 when the number of photons is low. In our sample the use of the Cash statistic generally results in a best-fit temperature that is a few percent higher than that measured with χ^2 .

We measure the core subtracted temperature T_{XCS} by extracting spectra with the same maximum radius as described above, but excluding the inner $0.2r_{500}$; the core subtracted temperature and the $0.2r_{500}$ exclusion radius are measured iteratively until convergence. (Our definition of r_{500} is given in § 3.5.) For two clusters, ZwCl 1356+6245 and CLG J0647+7015, the iteration does not converge to a reasonable value when the core is excluded, and so we do not measure core subtracted quantities for those two clusters.

Our measured values for the temperature of the entire cluster, and for T_{XCS} measured assuming self-similar evolution and assuming no evolution, are given in Table 6.

3.4. Comparison with Published Temperatures

Though calibrations continue to improve, measurements of the same cluster by different instruments, and by different methods with the same instruments, lead to temperature measurements that differ. To check the accuracy of our own temperature measurements, we compare our values to those obtained in two other recent *Chandra* studies.

Balestra et al. (2007) (hereafter Ba07) studied 56 clusters over a redshift and temperature range similar to our own; our samples have 38 clusters in common. Our data reduction and spectral fitting processes differ from theirs in several small ways: Ba07 use local backgrounds exclusively, while we, as described above, use blank-sky backgrounds when local backgrounds are not possible or give worse spectral fits; they always fix the value of N_{H} to galactic, while we allow it to float when the value obtained thereby is reasonable; they use a spectral extraction band of 0.6–8 keV, versus our 0.5– or 0.7–9 keV; and they include a spectral component to compensate for Ir-M edge residuals, a correction that has been taken into account in the more recent calibration files which we use. Because clusters are not isothermal, the emission-weighted mean temperature is affected by the choice of energy band. Most importantly, Ba07 use spectral extraction regions determined via a method intended to maximize the S/N , which results in the use of extraction radii up to a factor of two smaller than ours. Their resulting extraction regions have a clear redshift trend, with radii as small as $\sim 0.3 r_{500}$ at high redshift.

Maughan et al. (2007) (hereafter Ma07) measured temperatures for 115 clusters, of which 53 are in common with our sample. Differences between our analyses include their use of a 0.6–9.0 keV spectral fitting band; their fixing N_{H} to the galactic values; and their use of blank-sky backgrounds in some cases where we use local backgrounds, plus an additional soft X-ray background component. Ma07 also use a different method for determining the spectral extraction region, measuring all spectra out to a radius of r_{500} as determined from an iterative procedure using a mass- Y_{X} relation, where Y_{X} is the product of the temperature and gas mass (Kravtsov et al. 2006).

To examine the difference between our temperatures and those of these two studies, we compare the error-weighted ratio of our temperatures to theirs. Overall, our temperatures are *lower* than those of Ba07 by a weighted average of $(3 \pm 1)\%$, and *higher* than those of Ma07 by $(6 \pm 1)\%$. To examine whether we can reproduce their values, we remeasured the temperatures of five clusters using methods similar to those of Ba07 and Ma07; i.e., we used their reported aperture radii, spectral extraction bands, and spectral models. We fixed N_{H} in all cases for this comparison, but did not change our choice of background strategies. As can be seen in Table 1, these changes resulted in generally higher temperatures when using the methods closer to those of Ba07, and generally lower temperatures when using methods closer to those of Ma07, thus at least partially explaining the sources of systematic differences between our measurements and those of these two papers. Note that this does not mean that our temperatures necessarily came to agree more closely with theirs; for MS 0451.6-0305, for example, our initial temperature was higher than that of Ba07, and these changes resulted in an even higher temperature.

The overall hotter temperatures that we measure relative to Ma07 may be attributable to variations in ICM temperature with radius. As shown in §3.3, our spectral extraction radii average $(0.84 \pm 0.20)r_{500}$, while Ma07 uses uniform radii of r_{500} . The ICM temperature generally decreases with radius at these radii (e.g., Vikhlinin et al. 2005; Pratt et al. 2007), and so we would expect our measured temperatures to be systematically slightly higher than those of Ma07.

However, the differences between our temperature measurements and those of the other two studies are not uniform; there are dependences on temperature and, for Ba07, redshift. The left panel of Figure 3 shows the ratio of our temperatures to the literature values versus our temperature. In the case of the Ma07 comparison, the ratio is clearly greater at higher temperatures; a one-dimensional least-squares fit of a straight line shows that the ratio increases as $(0.14^{+0.12}_{-0.19}) \log T_{\text{X}}$ for Ba07, and as $(0.22^{+0.05}_{-0.09}) \log T_{\text{X}}$ for Ma07. The latter trend may again result from Ma07's choice of r_{500} as an extraction radius; extraction regions of hotter clusters may include more background-dominated area, leading to temperature systematics as parts of the spectrum are deweighted by background noise.

The right panel of Figure 3 shows the dependence of temperature ratio on redshift. There is no evidence for a redshift dependence when comparing to Ma07; the ratio varies as $(0.02 \pm 0.09)z$. For Ba07, however, the ratio

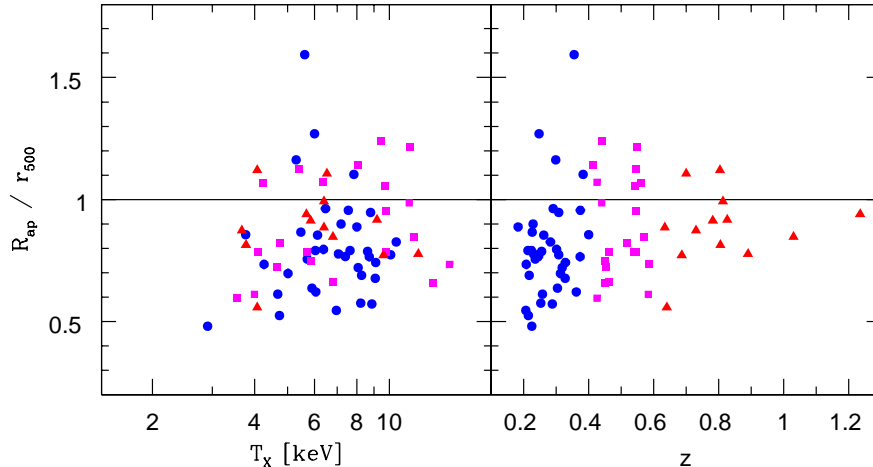


FIG. 2.— The ratio of our spectral extraction radius to r_{500} (defined as described in §3.5) for each cluster, plotted versus the measured non-core subtracted temperature (*left*) and versus redshift (*right*). Markers correspond to $z < 0.4$ (circles), $0.4 < z < 0.6$ (squares), and $z > 0.6$ (triangles).

TABLE 1
COMPARISON OF TEMPERATURE MEASUREMENTS

Cluster	z	Our T_X (keV)	Balestra et al. (2007)		Maughan et al. (2007)	
			They (keV)	We ^a (keV)	They (keV)	We ^a (keV)
MS 0451.6-0305	0.54	9.8 ± 0.8	$8.2^{+0.4}_{-0.3}$	10.5 ± 0.7	$6.7^{+0.6}_{-0.5}$	8.1 ± 0.4
ClG J1149+2223	0.54	9.8 ± 0.8	$12.9^{+1.2}_{-1.0}$	$9.9^{+1.0}_{-0.8}$	$8.4^{+0.9}_{-0.7}$	$8.7^{+0.9}_{-0.6}$
ClG J1120+2326	0.56	$4.2^{+0.6}_{-0.3}$	5.2 ± 0.5	$4.4^{+0.4}_{-0.3}$	$3.8^{+0.4}_{-0.3}$	3.2 ± 0.3
ClG J1113-2615	0.73	$3.7^{+0.6}_{-0.5}$	$5.7^{+0.9}_{-0.6}$	$5.0^{+0.9}_{-0.8}$	$3.8^{+0.9}_{-0.7}$	3.1 ± 0.4
RX J1317+2911	0.81	$3.8^{+1.7}_{-0.9}$	$4.5^{+1.4}_{-1.0}$	$4.4^{+0.9}_{-1.0}$	$2.0^{+0.7}_{-0.5}$	$3.3^{+1.5}_{-0.8}$

^a Our measurement of the cluster temperature using the same aperture and similar methods as the literature sources; see text.

varies as $(-0.31^{+0.09}_{-0.08})z$, showing a clear negative dependence on redshift. This is almost certainly a result of Ba07’s use of extraction regions that feature a trend toward smaller fractions of the virial radius at higher redshift.

The differences between our measured temperatures and those from the literature underscore the difficulties inherent in comparing cluster parameters measured using differing instruments, instrumental calibrations, and methods. This calls into question the reliability of results obtained from directly combining data from multiple studies (e.g., Branchesi et al. 2007), and suggests that caution should be taken when comparing more processed results, such as the low-redshift slopes and normalizations often combined with new measurements of higher-redshift clusters to test for scaling relation evolution (e.g., Vikhlinin et al. 2002; Ettori et al. 2004b; Kotov & Vikhlinin 2005).

3.5. Imaging Analysis

We extract X-ray images and use the spectral fit to obtain the conversion factor from counts to physical units in the rest frame 0.5–2 keV band. Because the flattening of statistical backgrounds using the exposure map generated for a particular observation results in a spatially inhomogeneous background image, we fit a flat background to the regions outside of the cluster emission using the same technique used to determine the surface brightness

profile, described below. The results of this fitting are checked by examining radial brightness profiles and via simple comparison of total counts in regions well outside of cluster emission.

As our observations do not in general contain enough photons to do a deprojection analysis, particularly at high redshift, we fit the standard spherical β model (Cavaliere & Fusco-Femiano 1978) to the cluster emission:

$$I(r) = I_0 \left[1 + \left(\frac{r}{R_c} \right)^2 \right]^{-3\beta+1/2}, \quad (5)$$

with central brightness I_0 , core radius R_c , and power-law index β . In what are traditionally considered “cool core” clusters, i.e., where there is a central emission excess due to the formation of a cool dense core, we fit a double β model (Ikebe et al. 1996, 1999; Mohr et al. 1999) with both components having the same center coordinates and index β , so that the total surface brightness is the sum of the two, i.e.,

$$I(r) = \sum_{i=1}^2 I_{0,i} \left[1 + \left(\frac{r}{R_{c,i}} \right)^2 \right]^{-3\beta+1/2}. \quad (6)$$

We fit these surface brightness profiles to the two-dimensional surface brightness images, and find the best fit and one σ confidence intervals for each parameter us-

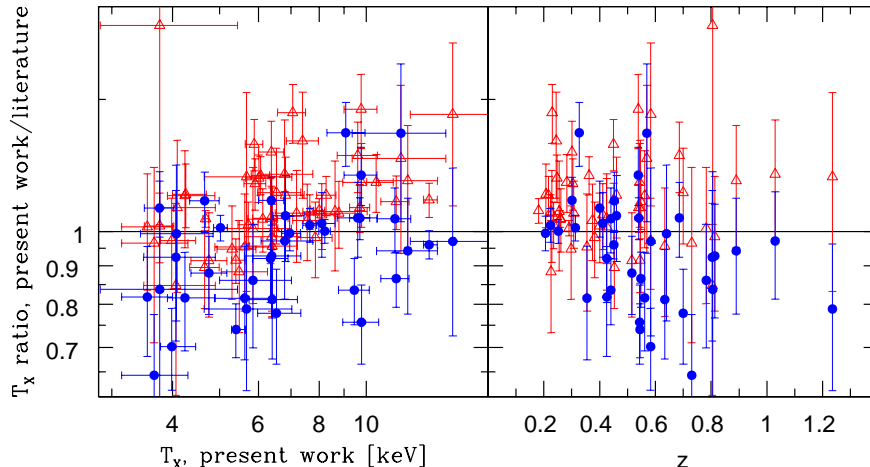


FIG. 3.— The ratio of our measured cluster temperatures to published temperatures (vertical axis), plotted versus our temperature (*left*) and versus redshift (*right*). Published temperatures are from Maughan et al. (2007) (triangles) and Balestra et al. (2007) (circles).

ing the Cash statistic. In a few cases (A521, A1682, and A2744) there are prominent clumps or subclusters separate from the main body of the cluster, which are masked out before fitting. In two cases we fix the value for β : A521, a multiply-merging cluster (Ferrari et al. 2003), for which we find a somewhat stable value of $\beta = 0.75$, which we adopt over the values of $\beta > 3$ which are found by a full gridding analysis; and ClG J1056-0337, a merging system (Jee et al. 2005) for which we find only very high values of β , leading us to adopt the canonical $\beta = 0.67$. In both cases we then measure 2σ uncertainties in the other fit parameters. The β model parameter fit results are listed in Table 7. The second, bright central component is, where used for a given cluster, listed as the second brightness and core radius components I_2 and $R_{c,2}$.

We measure several different cluster observables, each of which—X-ray luminosity, ICM mass, isophotal size, and mean ICM temperature—derives from the underlying cluster structure in a different way; by studying the evolution of multiple observables, we are examining the evolution of the ICM in multiple ways. Luminosity and ICM mass are measured within two different virial radii r_δ , which permits us to examine evolution on different scales within a cluster. We determine r_{500} and r_{2500} from the cluster temperature using M_δ – T_X relations determined by Arnaud et al. (2005) using XMM-*Newton* observations of local galaxy clusters. We use their relations for clusters with $T_X > 3.5$ keV:

$$r_{500} = 1.129 \left(\frac{T_X}{5 \text{ keV}} \right)^{0.497} E(z)^{-1} \text{ Mpc}, \quad (7)$$

$$r_{2500} = 0.501 \left(\frac{T_X}{5 \text{ keV}} \right)^{0.503} E(z)^{-1} \text{ Mpc}. \quad (8)$$

Note that by using virial radii obtained in this manner, we are implicitly testing the evolution of these local mass–temperature relations along with our other observables. That is, our “self-similar evolution” scenario includes evolution of the r_δ – T_X relations as written above, and the “no evolution” scenario includes no evolution (i.e., no $E(z)$ factor) in the r_δ – T_X relations.

We measure the projected X-ray luminosity L_X in the rest frame 0.5–2 keV band from the images described above, within radii of r_{500} and r_{2500} ; we also measure core subtracted luminosities L_{XCS} by excising the projected luminosity from the central $0.2r_{500}$. Luminosity measurements are centered on the cluster brightness peak, with the exception of A521, where we use the peak brightness of the main cluster, not the brighter infalling subcluster to the north of the cluster center (see, e.g., Ferrari et al. 2006); and ClG J1056-0337, where we use the western brightness peak, which has been identified as the “central” mass peak via weak lensing (e.g., Jee et al. 2005). Given the small field of view of Chandra, the virial radii r_δ often extend beyond the image boundary; furthermore, some observations are not deep enough that there is signal measurable out to a given r_δ . We thus establish for each cluster a maximum radius from the brightness peak at which either the detector edge is reached or the S/N falls close to unity; in a few cases the maximum radius is determined by the presence of other structure, as in the cases of ACO 2246 and ClG J1701+6414, which lie a small angular distance from one another in the same observation. Then, if the radius r_δ exceeds this established maximum radius for a given luminosity measurement, we do not carry out that measurement on that particular cluster; this is reflected in Tables 8 and 9, where luminosity measurements are not given in many cases. We include in the luminosity uncertainties contributions from the temperature used in calculating r_δ , as well as a uniform 10% background uncertainty.

The X-ray luminosity within a given radius can be modeled analytically by an integral of the ICM density profile and X-ray emissivity out to that radius. We can therefore use a measurement of the actual luminosity together with the measured β model parameters and the cluster temperature to find the central ICM density, and hence ICM mass via an integral of the density function to a given radius of interest; for details see Mohr et al. (1999). We estimate uncertainties on M_g by including the statistical uncertainties on the β model fit; a uniform 10% background uncertainty in the luminosity measure-

ment; and temperature uncertainties in r_δ . The ICM mass measurement is not subject to the same maximum radius restriction as luminosity, as the luminosity within any given radius can be used to measure the central density; while larger luminosity measurement radii are of course preferable, it is not necessary to measure the flux out to a given r_δ for an ICM mass measurement within that radius. Note that we do not similarly use the β model to extrapolate luminosity measurements out to a radius of interest; this is because we prefer to directly use projected luminosities without assumptions as to the structure of the cluster, but ICM mass cannot similarly be measured without such assumptions.

We measure the isophotal size R_I of a cluster by measuring the area A_I enclosed by an isophote I , and finding the effective radius given by $A_I = \pi R_I^2$. For these measurements we use images that have been adaptively smoothed using the CIAO task `csmooth`. We include the 10% background uncertainty in the R_I uncertainties by remeasuring at isophotes increased and decreased by the background uncertainty. In the 0.5–2 keV band we are using here, the conversion from X-ray counts to physical units varies slowly with cluster temperature, so we do not include temperature uncertainties in the isophotal size. We measure R_I at three different isophotes, 1.5×10^{-13} , 6×10^{-14} , and 3×10^{-14} erg s $^{-1}$ cm $^{-2}$ arcmin $^{-2}$ (in the rest frame 0.5–2 keV imaging band), which, like using both r_{500} and r_{2500} for the luminosity and ICM mass, lets us study evolution of R_I on different scales within a cluster. Clusters can “fall off” an isophotal size–temperature scaling relation when the isophote used approaches the peak surface brightness of the cluster; we therefore exclude clusters when their measured isophotal size is less than $0.2r_{500}$, our adopted core exclusion region.

3.6. Fitting Procedures

For a given relation involving an observable \mathcal{O} , we fit the form

$$\mathcal{O} = A \left(\frac{T_X}{6 \text{ keV}} \right)^\alpha (1+z)^\gamma, \quad (9)$$

or, in log space,

$$\log \mathcal{O} = \log A + \alpha \log \left(\frac{T_X}{6 \text{ keV}} \right) + \gamma \log(1+z). \quad (10)$$

That is, we fit a power-law temperature dependence α , power-law redshift dependence γ , and A , the normalization at zero redshift and temperature 6 keV.

In this paper we use unweighted orthogonal fits, meaning that we minimize the sum of the square of the point-line orthogonal distances, i.e., the sum

$$\sum_i \left\{ \frac{\log \mathcal{O}_i - [\log A + \alpha \log(T_{X,i}/6) + \gamma \log(1+z_i)]}{(1+\alpha^2)^{1/2}} \right\}^2. \quad (11)$$

Note that the form for redshift evolution assumed here is evolution of the normalization only, and so there is no factor of γ in the denominator. We determine 1σ uncertainties via bootstrap sampling; the best-fit value given in this paper is the mode of a histogram constructed from

the bootstrapping results, and the 1σ confidence interval is constructed in the usual manner so as to contain 68.3% of the counts around this mode. We also give here the RMS scatter in the vertical dimension (e.g., in L_X in the L_X – T_X relation) for the best-fit parameters; this one-dimensional scatter is a more intuitively understandable quantity than the orthogonal scatter, as it reflects the scatter in an observable (L_X , M_g , R_I) at a given temperature. We refer to this as the intrinsic scatter (σ_{int}), as the measurement uncertainties are generally much smaller than the total scatter in these relations (e.g., O’Hara et al. 2006).

The question of which fitting method is “best” is still open, and rests to a large extent on whether one property (such as T_X) is considered more fundamental than the other (such as L_X); this often seems implicit in discussions of L_X – T_X , M_g – T_X , and other relations, and would imply that a one-dimensional least-squares fit, with temperature (the lowest scatter mass estimator) as the independent variable, might be appropriate. But if both observables are considered to be linked via another property of the system (such as cluster mass), then a orthogonal minimization fit, which treats both variables equally, may be more appropriate; we take this view, and so adopt orthogonal fitting in this paper.

Fits of mock scaling relations using both the orthogonal fitting method and an ordinary least-squares (OLS) fit support this decision. A difficulty that arises in such tests is that assumptions must be made regarding the scatter in mock relations; e.g., if only scatter in the y direction is generated, then an OLS fit will doubtless give better results than an orthogonal fit. For example, Lopes et al. (2006) make the claim that orthogonal regression produces more accurate measurements of scaling relation slopes than the bisector method (discussed below), based on their own tests using mock data sets; however, as these data sets were generated using orthogonal scatter, such a result is entirely expected. Because of the difficulty in defining “correct” scatter, we test scenarios in which only scatter in the y direction is used, and in which equal scatter in both the x and y directions is used. That is, we generate a random x value, use an assumed scaling relation to find y , and then shift the values using normal random deviates in the y direction only, or in both the x and y directions. Note that using equal x and y scatter is *not* the same as using orthogonal scatter, and so an orthogonal relation should not be *a priori* assumed to give the correct result in such a case. In our testing we do not assume measurement uncertainties, but fit an intrinsic scatter in the y direction in the OLS fits so that the reduced χ^2 value is equal to unity. Again, in real scaling relations the scatter is generally dominated by intrinsic scatter, so this is a reasonable approach.

The results of our tests clearly indicate that the OLS method is a less robust approach than the orthogonal method. For example, when using only y direction scatter of 0.05 (i.e., the random deviates have a standard deviation in \log_{10} space of 0.05), the orthogonal method gives a result that is 2% ($\sim 1\sigma$) high while the OLS method gives the correct result; but when using equal scatter of 0.05 in x and y , the orthogonal method gives the correct slope, while the OLS method gives a result that is $\sim 10\%$ ($\sim 2\sigma$) too low. The results get worse for OLS more rapidly than for orthogonal fitting; e.g., scat-

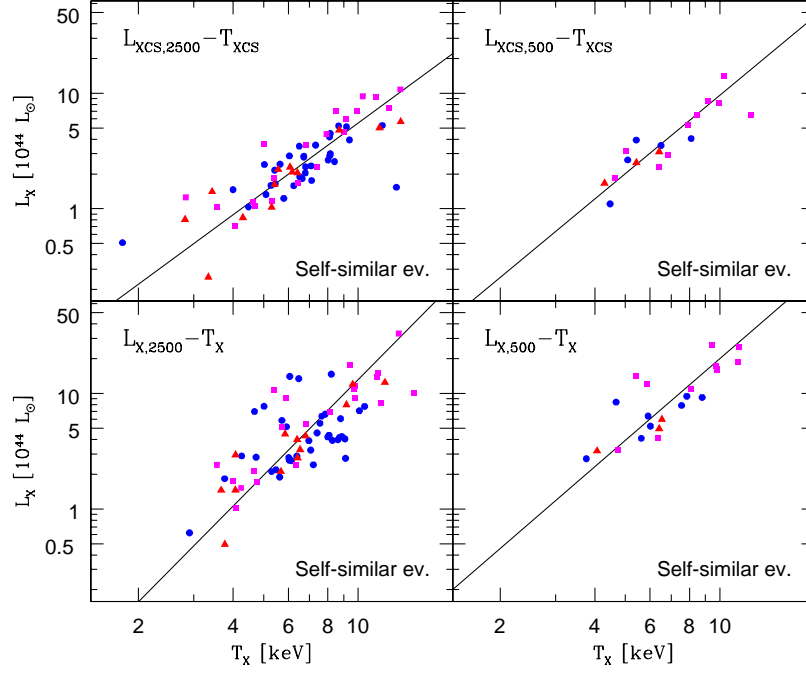


FIG. 4.— Projected X-ray luminosity within r_{2500} (left) and r_{500} (right), with non-core subtracted (top) and core subtracted (bottom) quantities, plotted versus temperature. These quantities are measured assuming *self-similar evolution*. Luminosity values are scaled to $z = 0$ using the best-fit redshift scaling for each relation, and the best-fit slope is plotted for each relation. Markers correspond to $z < 0.4$ (circles), $0.4 < z < 0.6$ (squares), and $z > 0.6$ (triangles).

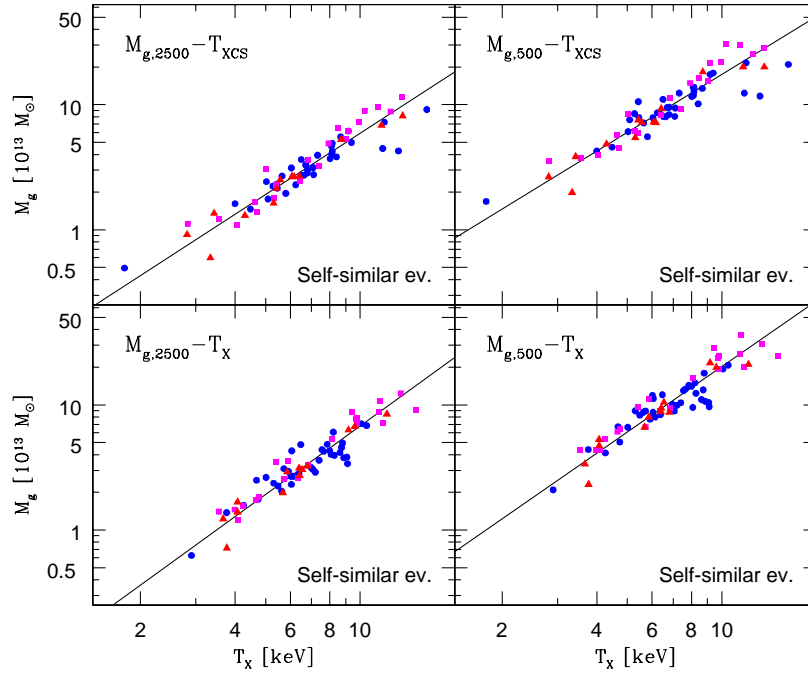


FIG. 5.— Same as Figure 4, but for $M_{\text{g}}-T_{\text{X}}$ relations.

ter of 0.15 in y only gives an orthogonal slope that is 16% ($\sim 2.5\sigma$) high, but scatter of 0.10 in both dimensions gives an OLS result that is 51% ($\sim 8.5\sigma$) too low. The results are very similar when true orthogonal scatter is used, rather than random, but on average equal, scatter in each dimension.

Again, the exact origin of scaling relation scatter is unknown, so it is difficult to declare a “correct” way of testing fitting methods. There is undoubtedly some measurement scatter, however, and so scaling relations certainly have at least some scatter in both dimensions. For this reason, as well as the physical arguments given above, we adopt the orthogonal fit as our chosen method for this paper.

Besides orthogonal fitting, another approach that treats the two variables equally is the bisector method, in which OLS fits are done with each of the two variables as independent and dependent (i.e., y as a function of x , and x as a function of y), and the final result bisects the two individual fits. This is not appropriate for our work, because we fit observables as a function of both temperature and redshift, and it is unclear how the bisector method can be extended into three dimensions. Orthogonal fitting is clearly defined in any number of dimensions; i.e., it seeks the shortest point-line distance in two dimensions, the shortest point-plane distance in three dimensions, and so forth. Also, each individual OLS fit in the bisector method is subject to the great dependence on the form of scatter as discussed above, and so the bisector method’s utility for studying scaling relations is likewise questionable.

4. TESTS OF THE SELF-SIMILAR EVOLUTION SCENARIO

We now examine the evolution of scaling relations while assuming self-similar evolution, as discussed in the introduction. That is, we assume that r_δ scales as $E(z)^{-1}$ when measuring L_X and M_g , and when determining the core subtraction radius for T_{XCS} and L_{XCS} . Our values for L_X and M_g , measured using the non-core subtracted temperature, are given in Table 8. We then test whether scaling relations evolve in a manner consistent with self-similar evolution.

4.1. Scaling Relations

The L_X – T_X and M_g – T_X scaling relations are plotted in Figures 4 and 5, respectively. In these figures the observables are scaled to $z = 0$ using the best-fit scaling relations. One qualitative feature of note is that the scatter is clearly smaller in the L_{XCS} – T_X relations than in their non-core subtracted counterparts; a similar, though smaller effect is visible in the ICM mass relations. This difference in scatter arises from biases in both temperature and the other observable in each relation induced as a result of cool core-related phenomena (e.g., Fabian et al. 1994; Markevitch 1998; O’Hara et al. 2006). Another interesting feature is the shallowness of the $L_{XCS,2500}$ – T_{XCS} relation compared to the non-core subtracted $L_{X,2500}$ – T_X relation. Best-fit scaling relation parameters are given in Table 2.

Studies of scaling relation evolution commonly fix the slopes to values measured from local samples, and fit only for an evolution factor. Because we are fitting all parameters simultaneously, we need to compare our measured slopes to those of local samples. Our $L_{X,2500}$ – T_X

relation and $L_{X,500}$ – T_X relation have slopes of $2.75^{+0.28}_{-0.26}$ and $2.35^{+0.33}_{-0.24}$, respectively, which are significantly higher than the self-similar expectation $\alpha = 2$, as has been generally observed in low-redshift samples (e.g., Markevitch 1998); note that using luminosities from a fixed energy band as done here (rest frame 0.5–2 keV) gives a somewhat lower slope than the more commonly used bolometric luminosities, as shown by, e.g., Zhang et al. (2007). For the $M_{g,2500}$ – T_X relation we find $\alpha = 1.82 \pm 0.08$, in good agreement with $\alpha = 1.91 \pm 0.16$ found by Ettori et al. (2002) using *BeppoSAX* data and a bisector fit; for the $M_{g,500}$ – T_X relation we find $\alpha = 1.74 \pm 0.09$, in fair agreement with $\alpha = 1.98 \pm 0.11$ measured by Mohr et al. (1999) using *ROSAT* PSPC images and a mixture of *Einstein*, *Ginga*, and *ASCA* temperatures, with an unweighted orthogonal fit. Both of these are significantly higher than the self-similar expectation $\alpha = 1.5$.

In all cases, the scaling relations with core subtracted quantities have shallower slopes than the standard relations. Remarkably, the core subtracted relations have slopes consistent with the self-similar expectation to within 1σ , the sole exception being $M_{g,2500}$ – T_{XCS} , which is consistent to within 2σ .

4.2. Evolution with Redshift

Figure 6 shows the ratio of observables (L_X and M_g) to the self-similar expectation, plotted versus redshift. That is, the vertical axis is the ratio of the observed value to the self-similar prediction using the appropriate fit in Table 2 and the cluster temperature and redshift. The horizontal line in each plot therefore marks the self-similar expectation. Plotting in this way shows deviations from the self-similar redshift evolution prediction as a redshift dependence of the ratio $\mathcal{O}_i/\mathcal{O}_{\text{fit}} = 0$; we also plot the best-fit value of γ for each relation, showing how the normalization of each scaling relation in fact evolves.

For each scaling relation, Table 2 includes the percent significance by which each relation differs from zero, i.e., the significance of its deviation from the self-similar prediction. Because the distributions of γ are not in general normal, this significance is determined using binned data to measure the probability density at $\gamma = 0$, and integrating to the same probability density on the other side of the peak value. Because we use binned data to estimate this parameter, it can be determined most precisely when γ is significantly different from zero; hence, we quote only at 1% precision for values less than 99%.

All luminosity– and ICM mass–temperature scaling relations have $\gamma < 0$ at greater than the 1σ level. There is clearly an overall tendency for relations to evolve more slowly than expected from the self-similar prediction, i.e., $\gamma < 0$. We can combine multiple probabilities by assuming independence of the scaling relations; though all of the measured properties are of course linked to some extent by their dependence on the underlying ICM structure, X-ray luminosity and ICM mass depend on that structure in very different ways, and the two virial radii which we use probe two rather different regions of the cluster (i.e., r_{500} comes close to looking at the cluster as a whole, while r_{2500} measures a much smaller fraction that is more dependent on core structure and evolution). Combining the results for all four core subtracted relations by multiplying the given probabilities of consistency

TABLE 2
FIT PARAMETERS ASSUMING SELF-SIMILAR EVOLUTION

Core Subtracted Relations					
Relation	α	A^a	γ	Diff. from 0 (%) ^b	σ_{int}^c
$L_{\text{XCS},2500}-T_{\text{XCS}}$	$2.00^{+0.23}_{-0.19}$	$2.00^{+0.35}_{-0.30}$ E44	$-0.86^{+0.38}_{-0.36}$	95–	0.28 ± 0.05
$L_{\text{XCS},500}-T_{\text{XCS}}$	$2.26^{+0.29}_{-0.33}$	$3.02^{+1.35}_{-1.24}$ E44	$-1.28^{+1.28}_{-0.86}$	69–	$0.21^{+0.08}_{-0.07}$
$M_{g,2500}-T_{\text{XCS}}$	$1.63^{+0.09}_{-0.08}$	$2.57^{+0.18}_{-0.17}$ E13	$-0.35^{+0.20}_{-0.15}$	90–	$0.00^{+0.05}_{-0.00}$
$M_{g,500}-T_{\text{XCS}}$	1.56 ± 0.10	$7.94^{+0.06}_{-0.05}$ E13	$-0.24^{+0.20}_{-0.18}$	74–	0.09 ± 0.04
Non-Core Subtracted Relations					
Relation	α	A^a	γ	Diff. from 0 (%) ^b	σ_{int}^c
$L_{\text{X},2500}-T_{\text{X}}$	$2.75^{+0.29}_{-0.26}$	$3.24^{+0.75}_{-0.61}$ E44	$-1.50^{+0.42}_{-0.49}$	99.4–	$0.60^{+0.08}_{-0.09}$
$L_{\text{X},500}-T_{\text{X}}$	$2.35^{+0.33}_{-0.24}$	$6.03^{+3.75}_{-2.22}$ E44	$-1.90^{+1.17}_{-1.11}$	90–	$0.39^{+0.12}_{-0.10}$
$M_{g,2500}-T_{\text{X}}$	1.82 ± 0.08	$2.69^{+0.19}_{-0.18}$ E13	$-0.55^{+0.17}_{-0.15}$	99.4–	0.14 ± 0.02
$M_{g,500}-T_{\text{X}}$	1.74 ± 0.09	$8.32^{+0.59}_{-0.56}$ E13	$-0.45^{+0.18}_{-0.16}$	98–	0.13 ± 0.02

^a In units of L_{\odot} for $L_{\text{X}}-T_{\text{X}}$ relations, M_{\odot} for $M_{\text{g}}-T_{\text{X}}$ relations. ^b Significance level at which γ differs from zero, as determined by bootstrap sampling and refitting; the sign indicates whether γ is positive (+) or negative (–). ^c Intrinsic scatter in L_{X} or M_{g} at fixed temperature, expressed in base e .

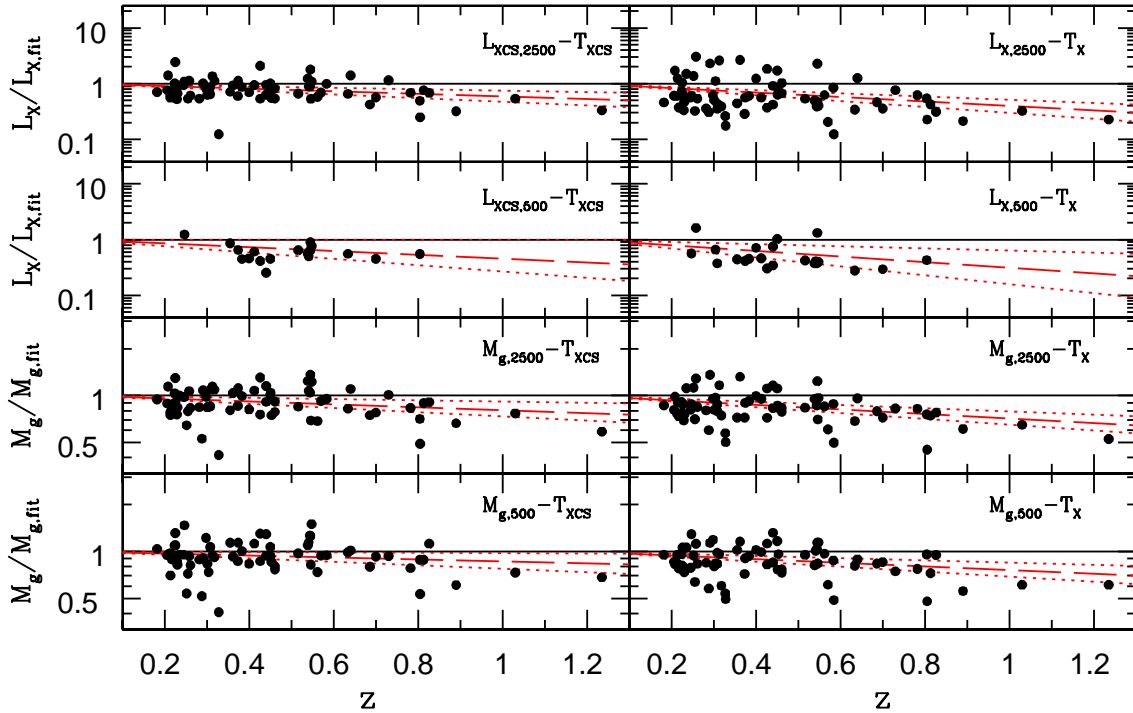


FIG. 6.— Ratio of measured observable (luminosity or ICM mass) to the best-fit observable–temperature scaling relation, plotted versus redshift. These measurements assume *self-similar evolution*. The horizontal line ($O/O_{\text{fit}} = 1$) corresponds to no evolution beyond the assumed self-similar evolution, i.e., $\gamma = 0$ in our notation. The dashed and dotted lines correspond to the best fit and 1σ boundaries on γ for each relation.

with zero gives a combined probability of $< 0.1\%$ that all four relations are consistent with the self-similar evolution scenario, ruling out pure self-similar evolution at greater than 3σ confidence. The same relations with non-core subtracted quantities have an even smaller probability (i.e., $\ll 0.1\%$) of consistency with zero.

We draw your attention to the $z > 0.8$ clusters in our sample because of the special leverage they have on our evolution results. Examination of Figure 6 suggests

no qualitative difference in the high-redshift population when compared to lower-redshift clusters. For these clusters to bias our results toward more negative evolution, it would require systematically selecting *underluminous* clusters, which is the opposite of what is expected.

The relations involving core subtracted quantities have more positive evolution than those involving non-core subtracted quantities. This could indicate a decrease in clusters with cool cores at higher redshifts, which is ex-

pected in the scenario wherein clusters form cool cores over time in the absence of major merging events. The evolution of the cool core fraction remains relatively unexplored; Bauer et al. (2005) found no evolution in the cool core fraction up to $z \sim 0.4$ using spatially resolved spectral analysis, but such an analysis is difficult to carry out at higher redshifts. Vikhlinin et al. (2006) used a measurement of the “cuspsiness” of the surface brightness distribution to count cool cores in a sample of clusters at $z > 0.5$, and found a fourfold decrease in the cool core fraction from $z=0$ to $z=0.5$, which might support the concept of cool cores indicating a “relaxed cluster” that has not undergone recent major mergers. This concept is being increasingly challenged, however, by results from simulations that ascribe the presence or lack of a cool core to aspects of cluster formation history such as preheating (McCarthy et al. 2004) or early major mergers (Burns et al. 2007), and observational evidence that cool core and non-cool core cluster populations differ in characteristics beyond their morphological state (O’Hara et al. 2006). Burns et al. (2007) specifically studied the redshift evolution of the cool core fraction, and find no change in the fraction up to $z \sim 1$ in simulations that successfully reproduce other aspects of cluster and core structure. Our results here may support the classical notion of cool cores evolving over time, in support of the Vikhlinin et al. (2006) results. Alternatively, a constant cool core fraction could still produce an apparent negative evolution in scaling relation normalization simply because cool cores in those clusters that do have them will tend to grow over time; such a result was reported in simulations by Kay et al. (2007). We further discuss possible evolution in scatter in § 8.

4.3. Summary of Self-Similar Evolution Results

X-ray luminosity and ICM mass at fixed temperature evolve more slowly than expected from the self-similar evolution model. This conclusion is supported by significant ($> 1\sigma$) negative evolutions in all L_X - and M_g - T_X scaling relations, and by combined constraints using multiple core subtracted or non-core subtracted relations that rule out self-similar evolution at $> 99.9\%$ confidence. The less negative evolution of the core subtracted relations suggests that the cool core fraction decreases with redshift, that cool cores grow over time, or a combination of the two.

5. TESTS OF THE NO EVOLUTION SCENARIO

We now examine the evolution of scaling relations while assuming no evolution, i.e., we assume no scaling in r_δ when measuring L_X and M_g , and when determining the core subtraction radius for T_{XCS} and L_{XCS} . Our values for L_X and M_g measured using the non-core subtracted temperature are given in Table 9. We do not measure $L_{X,500}$ or $L_{XCS,500}$ in this scenario, as only a handful of clusters have observations of sufficient exposure time and angular extent that we can measure out to the non-evolved r_{500} .

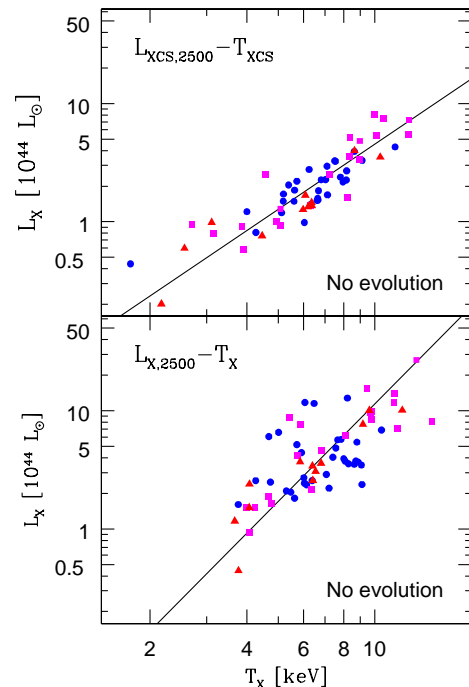


FIG. 7.— Projected X-ray luminosity within r_{2500} (left) and r_{500} (right), with non-core subtracted (top) and core subtracted (bottom) quantities, plotted versus temperature. These quantities are measured assuming *no evolution*. Luminosity values are scaled to $z = 0$ using the best-fit redshift scaling for each relation, and the best-fit slope is plotted for each relation. Markers correspond to $z < 0.4$ (circles), $0.4 < z < 0.6$ (squares), and $z > 0.6$ (triangles).

5.1. Scaling Relations and Their Evolution

The L_X - T_X and L_X - M_g relations are plotted in Figures 7 and 8, respectively. As in the self-similar evolution case, the slope of the luminosity–temperature relation decreases significantly when core-subtracted quantities are used, and the scatter likewise decreases for both the luminosity and the ICM mass relations. We give the best-fit scaling relation parameters from this scenario in Table 3, and plot the redshift evolution of the scaling relations in Figure 9.

The measured slopes and normalizations in this scenario are consistent with those measured in § 4, including the tendency for core subtracted relations to have shallower slopes than non-core subtracted relations. Also in common between the two scenarios is the tendency for core subtracted relations to have more positive evolution than non-core subtracted relations.

Single non-core subtracted relations are generally consistent with negative evolution, and core subtracted relations are generally consistent with positive evolution. Combining all three core subtracted relations gives a combined consistency with $\gamma = 0$ (i.e., with the predictions of the no evolution scenario) of 1%; for the non-core subtracted relations, the value is 8%.

5.2. Summary of No Evolution Scenario Results

The core subtracted scaling relations rule out the “no evolution” scenario at 99% confidence; non-core subtracted relations give less certain results. As in the self-similar evolution scenario, the core subtracted relations

TABLE 3
FIT PARAMETERS ASSUMING NO EVOLUTION

Core Subtracted Relations					
Relation	α	A^a	γ	Diff. from 0 (%) ^b	σ_{int}^c
$L_{\text{XCS},2500}-T_{\text{XCS}}$	$1.84^{+0.18}_{-0.14}$	$1.74^{+0.26}_{-0.22}\text{E44}$	$0.56^{+0.37}_{-0.35}$	88+	$0.24^{+0.04}_{-0.05}$
$M_{g,2500}-T_{\text{XCS}}$	1.57 ± 0.07	$2.40^{+0.17}_{-0.16}\text{E13}$	$0.20^{+0.20}_{-0.12}$	89+	0.00 ± 0.00
$M_{g,500}-T_{\text{XCS}}$	1.52 ± 0.08	$7.59^{+0.54}_{-0.51}\text{E13}$	$0.10^{+0.19}_{-0.17}$	41+	0.08 ± 0.04
Non-Core Subtracted Relations					
Relation	α	A^a	γ	Diff. from 0 (%) ^b	σ_{int}^c
$L_{\text{X},2500}-T_{\text{X}}$	$2.75^{+0.34}_{-0.25}$	$2.81^{+0.73}_{-0.58}\text{E44}$	-0.25 ± 0.56	36-	0.59 ± 0.09
$M_{g,2500}-T_{\text{X}}$	1.78 ± 0.08	$2.57^{+0.18}_{-0.17}\text{E13}$	$-0.10^{+0.17}_{-0.15}$	43-	0.13 ± 0.02
$M_{g,500}-T_{\text{X}}$	1.74 ± 0.10	$8.13^{+0.58}_{-0.54}\text{E13}$	$-0.25^{+0.19}_{-0.18}$	78-	0.14 ± 0.02

^a In units of L_{\odot} for $L_{\text{X}}-T_{\text{X}}$ relations, M_{\odot} for $M_{\text{g}}-T_{\text{X}}$ relations. ^b Significance level at which γ differs from zero, as determined by bootstrap sampling and refitting; the sign indicates whether γ is positive (+) or negative (-). ^c Intrinsic scatter in L_{X} or M_{g} at fixed temperature, expressed in base e .

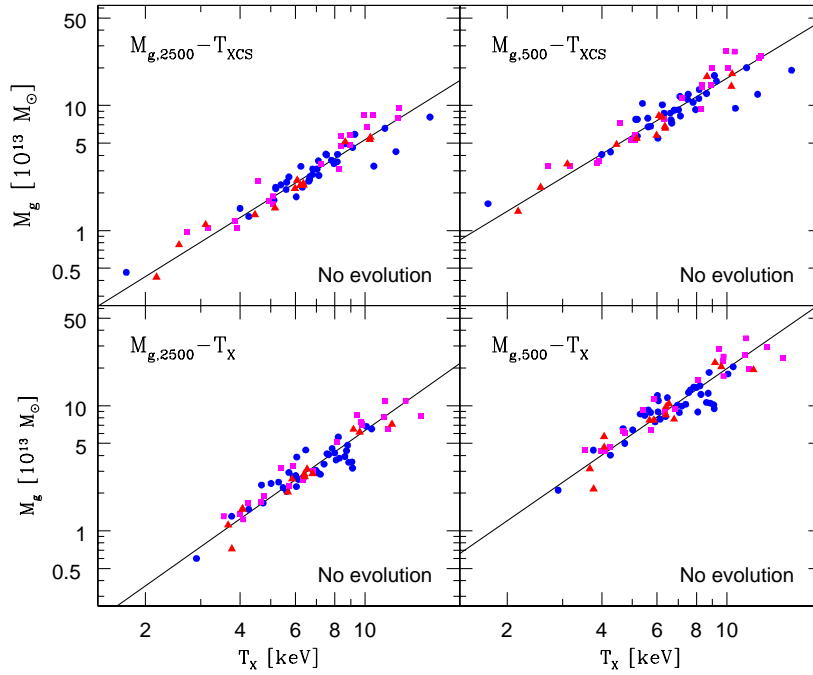


FIG. 8.— Same as Figure 7, but for $M_{\text{g}}-T_{\text{X}}$ relations.

have slopes that are consistent with self-similar expectations, and evolution that is more rapid than the corresponding non-core subtracted relations. Together with the results from the self-similar evolution tests, these findings indicate that cluster scaling relations do evolve, but they evolve less rapidly than the self-similar expectation.

6. TESTING EVOLUTION OF THE ICM FRACTION

One simple model for the evolution of cluster parameters such as L_{X} and M_{g} is a simple evolution of the gas mass fraction f_{g} , i.e., the ratio of the ICM mass to the total mass (baryons + dark matter) of a cluster. It is sometimes assumed in cosmological studies using clusters that f_{g} is constant with redshift if clusters are selected appropriately (e.g., Rines et al. 1999; Allen et al. 2004), but this assumption is difficult to test because of

degeneracies between f_{g} measurements and cosmological parameters. Simulations disagree on the baryon fraction evolution, with some claiming to see a negative evolution (e.g., Kay et al. 2007), while others find no evolution (e.g., Crain et al. 2007).

We can test whether our data are consistent with an evolution in f_{g} by directly combining measured values of γ for individual scaling relations. X-ray luminosity varies proportional to the square of the ICM density, and ICM mass is directly proportional to the ICM density. Because we are working in log space, this means that we combine $\gamma_{M_{\text{g}}}$ with $\gamma_{L_{\text{X}}}/2$. We use the core subtracted relations for this test because these relations are presumably less biased by cluster structural changes in the core, and therefore more sensitive to more global changes in the gas fraction.

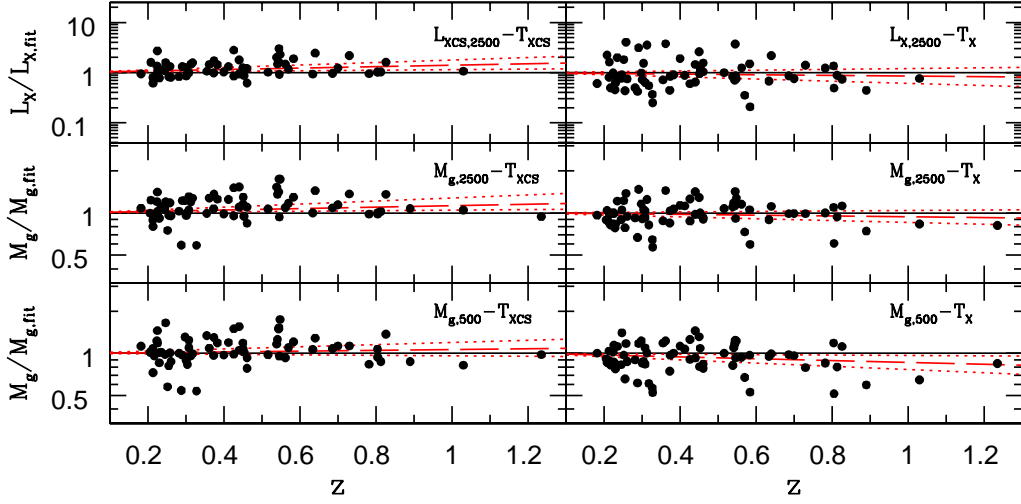


FIG. 9.— Ratio of measured observable (luminosity or ICM mass) to the best-fit observable–temperature scaling relation, plotted versus redshift. These measurements assume *no evolution*. The horizontal line ($O/O_{\text{fit}} = 1$) corresponds to no evolution, i.e., $\gamma = 0$ in our notation. The dashed and dotted lines correspond to the best fit and 1σ boundaries on γ for each relation.

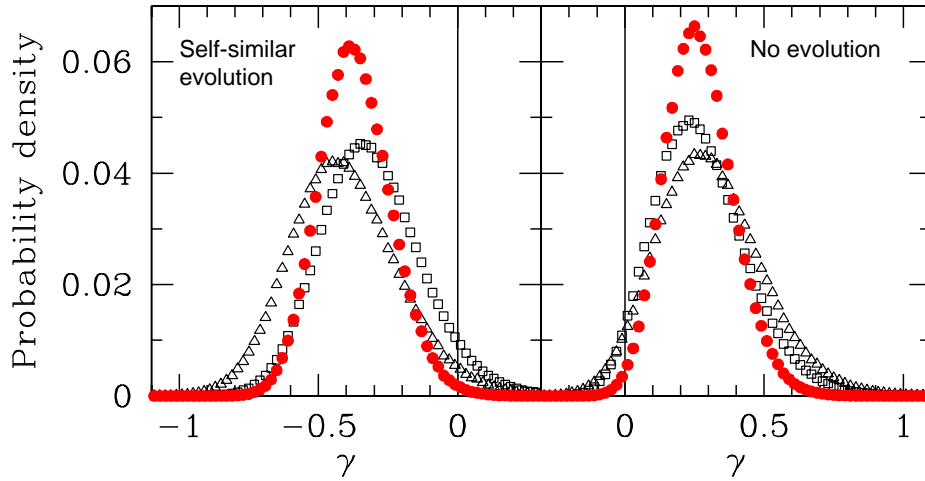


FIG. 10.— Constraints on the evolution of f_g for the self-similar evolution (*left*) and no evolution (*right*) scenarios. Open triangles are from the fit to the $L_{\text{XCS},2500}-T_{\text{XCS}}$ relation (with the values halved, as discussed in the text), open squares are from $M_{g,2500}-T_{\text{XCS}}$ relation, and filled circles are the normalized product of the two. The best-fit to the combined relations gives $\gamma_{f_g} = -0.39 \pm 0.13$ in the self-similar evolution scenario, and $\gamma_{f_g} = 0.25^{+0.12}_{-0.11}$ in the no evolution scenario.

First we examine the $L_{\text{XCS},2500}-$ and $M_{g,2500}-T_{\text{XCS}}$ relations measured in the self-similar evolution scenario. The left panel of Figure 10 shows histograms for the values of γ resulting from the bootstrap fitting of the $L_{\text{XCS},2500}-$ and $M_{g,2500}-T_{\text{X}}$ relations (triangles and squares, respectively; the values of γ for luminosity have been divided by 2 as explained above); the vertical axis has been scaled so that the values represent the probability of γ falling in each bin. The circles are the product of the two individual distributions, renormalized so that the total probability is unity. The data give a best fit value of $\gamma_{f_g} = -0.39 \pm 0.13$; the data are inconsistent with $\gamma_{f_g} = 0$ (i.e., a constant gas fraction) at the 99.1% level.

The right panel of Figure 10 shows data calculated in the same way, but in the no evolution scenario. In

this scenario we find the best-fit combined scaling to be $\gamma_{f_g} = 0.25^{+0.12}_{-0.11}$, and inconsistent with $\gamma_{f_g} = 0$ at the 98% level.

Our results are consistent with the evolution in L_X and M_g originating from a simple evolution in gas mass fraction. While such consistency does not prove this scenario, it is encouraging to note that the values of γ_{M_g} and $\gamma_{L_X}/2$ are quite similar in both scenarios, and evolution in f_g thus provides a consistent explanation for the evolution of these two different physical quantities. The most probable value $\gamma_{f_g} \simeq -0.4$ in the self-similar evolution scenario suggests a decrease of $\sim 25\%$ in f_g between redshifts 0 and 1, which would bias distance measurements that assume constant f_g at the $\sim 17\%$ level ($d_A \propto f_g^{2/3}$; e.g., Rines et al. 1999).

Note that we have measured the evolution of f_g specif-

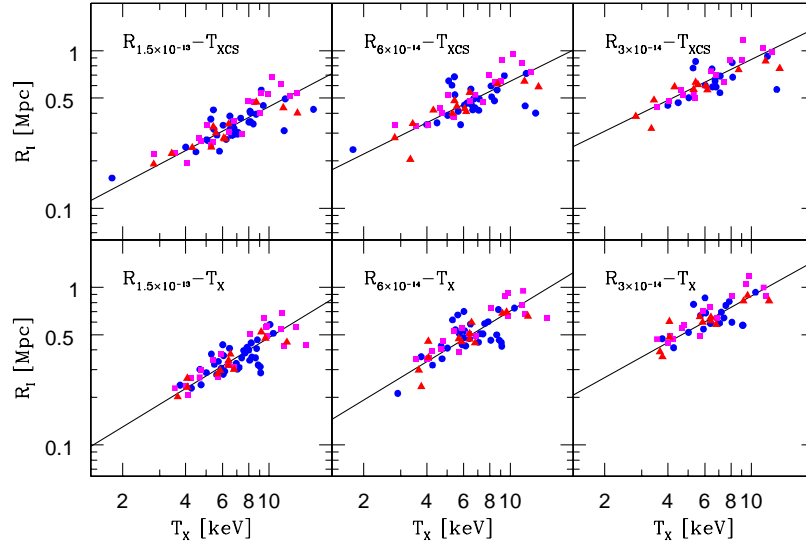


FIG. 11.— Isophotal size–temperature relations for non-core subtracted (top) and core subtracted (bottom) temperature; the isophote used decreases from left to right. Size values are scaled to $z = 0$ using the best-fit redshift scaling for each relation, and the best-fit slope is plotted for each relation. Markers vary by redshift as in Figure 4.

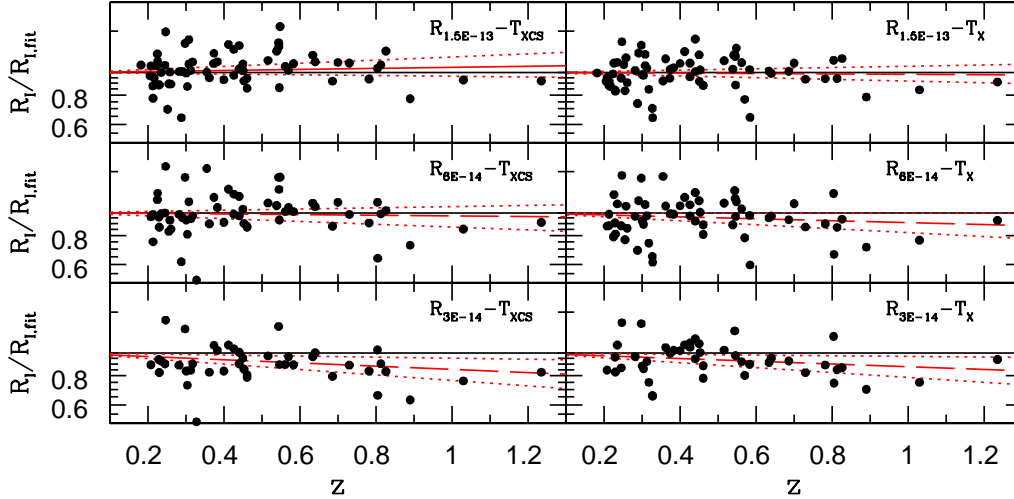


FIG. 12.— Ratio of measured isophotal size to the best-fit size–temperature scaling relation, plotted versus redshift. These measurements assume no evolution. The horizontal line ($R_I/R_{I,\text{fit}} = 1$) corresponds to no evolution, i.e., $\gamma = 0$ in our notation. The dashed and dotted lines correspond to the best fit and 1σ boundaries on γ for each relation.

ically within the radius r_{2500} . We do not attempt a similar measurement at r_{500} because of a lack of luminosity measurements at that radius in the no evolution scenario, and the very large uncertainties on the $L_{\text{XCS},500}$ – T_{XCS} relation in the self-similar evolution scenario. There is in both scenarios and in both core subtracted and non-core subtracted relations a tendency for $M_{g,500}$ to evolve more slowly than $M_{g,2500}$ (though only at the 0.5 – 1σ level); this is consistent with observations and simulations which find that the evolution in f_g decreases with increasing radius, with evolution nearing zero at the virial radius (e.g., Sadat et al. 2005; Ettori et al. 2006). This suggests that the distance biases associated with the assumption of constant gas fraction would be less severe if the X-ray data were deep enough to allow the measurements to be

made at or beyond the virial radius, which may be possible which future observatories such as *Constellation-X*.

7. EVOLUTION OF ISOPHOTAL SIZE

We now examine the evolution of isophotal size–temperature scaling relations. This is done separately from the previous “self-similar evolution” and “no evolution” because as discussed in § 2, for clusters that are described by a β model with $\beta = \frac{2}{3}$, the two scenarios give the same result (Mohr et al. 2000). That is, if the ICM is distributed as r^{-2} beyond the core, the size–temperature relation does not evolve with redshift. While this potentially makes the size–temperature relation useful as a means to study the evolution of the angular diameter distance, and hence as a tool for studying

TABLE 4
 FIT PARAMETERS FOR ISOPHOTAL SIZE RELATIONS

Core Subtracted Relations					
Relation	α	A (Mpc)	γ	Diff. from 0 (%) ^a	σ_{int} ^b
$R_{1.5 \times 10^{-13}} - T_{\text{XCS}}$	$0.70^{+0.07}_{-0.06}$	0.31 ± 0.02	$0.08^{+0.17}_{-0.14}$	42+	0.13 ± 0.02
$R_{6 \times 10^{-14}} - T_{\text{XCS}}$	$0.66^{+0.09}_{-0.08}$	0.46 ± 0.03	$-0.05^{+0.15}_{-0.18}$	33-	0.16 ± 0.02
$R_{3 \times 10^{-14}} - T_{\text{XCS}}$	0.65 ± 0.10	$0.63^{+0.05}_{-0.04}$	-0.26 ± 0.18	87-	$0.12^{+0.03}_{-0.02}$
Non-Core Subtracted Relations					
Relation	α	A (Mpc)	γ	Diff. from 0 (%) ^a	σ_{int} ^b
$R_{1.5 \times 10^{-13}} - T_{\text{X}}$	0.81 ± 0.07	0.32 ± 0.01	$-0.03^{+0.13}_{-0.11}$	13-	0.13 ± 0.01
$R_{6 \times 10^{-14}} - T_{\text{X}}$	0.81 ± 0.09	0.47 ± 0.03	-0.16 ± 0.16	68-	0.16 ± 0.02
$R_{3 \times 10^{-14}} - T_{\text{X}}$	$0.74^{+0.08}_{-0.07}$	$0.60^{+0.06}_{-0.04}$	-0.22 ± 0.17	79-	0.14 ± 0.02

^a Significance level at which γ differs from zero, as determined by bootstrap sampling and refitting; the sign indicates whether γ is positive (+) or negative (-). ^b Intrinsic scatter in R_I at fixed temperature, expressed in base e .

cosmology, it makes it less useful for constraining the evolution of the ICM and cluster structure as we have done with luminosity and ICM mass relations.

7.1. Scaling Relations and Their Evolution

Size-temperature scaling relations are shown in Figure 11; as with the previous scaling relation plots, these have had the measured redshift evolution projected out. Best-fit scaling relation parameters are given in Table 4. The slopes of the relations using core subtracted temperatures are consistent with the theoretical value $\alpha = \frac{2}{3}$ (Mohr et al. 2000), and the relations with non-core subtracted temperature are somewhat higher. Our fit slope for the $R_{3 \times 10^{-14}} - T_{\text{X}}$ relation is $0.74^{+0.08}_{-0.07}$, which differs significantly from the value $\alpha = 0.93 \pm 0.11$ found by Mohr et al. (2000) using *ROSAT* PSPC images and literature values for T_{X} .

Redshift evolution of the isophotal size relations is shown in Figure 12. For the fits to the entire sample, the isophotal size relations show little or no evolution in the isophote closest to the core, and a trend toward more negative evolution as the isophote used decreases, i.e., as one examines the cluster at distances further from the core.

Having shown in § 6 that the evolution in L_{X} and M_g with respect to the self-similar expectation can be modeled by a simple evolution in the gas fraction, we can check for consistency of that evolution with the isophotal size results. The brightness at a given cluster radius r is related to the gas fraction f_g as $I(r) \propto f_g^2$, and so it can be shown that for a cluster described by a spherical β model the measured isophotal size scales with $I(r)$ as $R_I \propto I(r)^{1/(6\beta-1)}$ (Mohr et al. 2000). Thus we expect

$$R_I \propto f_g^{2/(6\beta-1)}, \quad (12)$$

which, for the standard value of $\beta = \frac{2}{3}$ (e.g., Jones & Forman 1984; Mohr et al. 1999), means that isophotal size should scale as $f_g^{2/3}$. For our self-similar evolution measurement of $\gamma_{f_g} = -0.39 \pm 0.13$, this would predict $R_I \propto (1+z)^{-0.26 \pm 0.09}$, in good agreement with the directly measured evolution of $\gamma = -0.26 \pm 0.18$ in the $R_{3 \times 10^{-14}} - T_{\text{XCS}}$ relation, and of $\gamma = -0.05^{+0.15}_{-0.18}$ in the $R_{6 \times 10^{-14}} - T_{\text{XCS}}$ relation. More positive evolution at higher isophotes may be an indication of structural

changes as clusters evolve and the density profiles of clusters become more peaked at lower redshift.

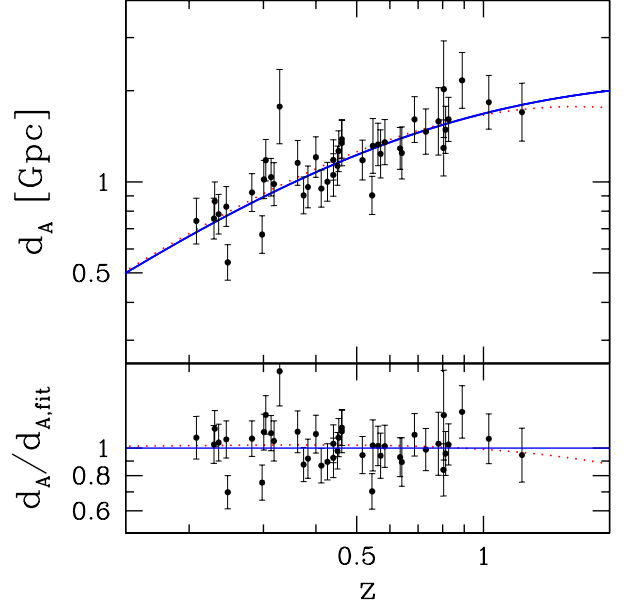


FIG. 13.— Measured angular diameter distance d_A plotted versus redshift for the $R_{3 \times 10^{-14}}$ sample. The solid line shows $d_A(z)$ for the best-fit measured cosmology $\Omega_M = 0.02$, $\Omega_\Lambda = 0.31$, and the dotted line shows $d_A(z)$ for our adopted cosmology $\Omega_M = 0.266$, $\Omega_\Lambda = 0.734$.

7.2. Prospects for Cosmology Using Isophotal Size

As mentioned above, the predicted non-evolution of R_I with redshift makes these size measurements a promising source of angular diameter distances, which can be used to constrain cosmological parameters. Such an undertaking is beyond the scope of this paper, but we sketch here the basic ideas underlying such a measurement.

If isophotal size indeed evolves in a manner predictable by the evolution in f_g , then one can use a measured angular isophotal size θ_I , together with a physical isophotal size R_I for the same cluster predicted from a scaling relation, to determine the angular diameter distance, $d_A = R_I / \theta_I$; this can then be used to measure the cosmological parameters which determine $d_A(z)$. As a test, we use θ_I measured from our $R_{3 \times 10^{-14}}$ sample, and use the

best-fit slope and normalization found for the $R_{3 \times 10^{-14}}-T_{\text{XCS}}$ relation to predict $R_I(T_X, z)$. Because we have found evolution in L_X and M_g which suggests evolution in f_g , we adopt the best-fit f_g evolution $\gamma_{f_g} = -0.39$ and its consequent isophotal size evolution $\gamma_{R_I} = -0.26$ in the size-temperature relation, as discussed above. Uncertainties in d_A are a combination of the temperature uncertainty and the measured intrinsic scatter in the $R_{3 \times 10^{-14}}-T_{\text{XCS}}$ relation.

Note that this is not simply an independent cosmological test. This is a consistency test where (1) an input cosmological model is assumed, (2) f_g evolution is measured using the evolution-sensitive L_X and M_g scaling relations, and (3) that evolution is adopted in using isophotal sizes to derive an output cosmology. Because the cosmological dependencies of each scaling relation differ, the input and output cosmologies will only agree for the correct model.

Figure 13 shows the angular diameter distance versus redshift, with our input cosmology and the output best-fit cosmology. As can be seen, these data do not reach redshifts high enough to place tight constraints on cosmology. Figure 14 shows confidence intervals for the density parameters Ω_M and Ω_Λ (we fix H_0 to our assumed value of $70.9 \text{ km s}^{-1} \text{ Mpc}^{-1}$). The uncertainties on both parameters are quite large; fully marginalized constraints are $\Omega_M = 0.02^{+0.49}_{-0.02}$, $\Omega_\Lambda = 0.31^{+0.59}_{-0.19}$. We do successfully recover our input cosmology within the 1σ region.

This combination of the use of L_X-T_X and M_g-T_X relations to constrain the evolution of the ICM, and R_I-T_X relations to measure distances is an approach that deserves further attention. As X-ray surveys that include spectroscopic temperature measurements push to higher redshifts, the use of isophotal sizes to measure angular diameter distances as demonstrated here should provide a new source of cosmological measurements, complementary to other cluster methods and to CMB and supernova constraints.

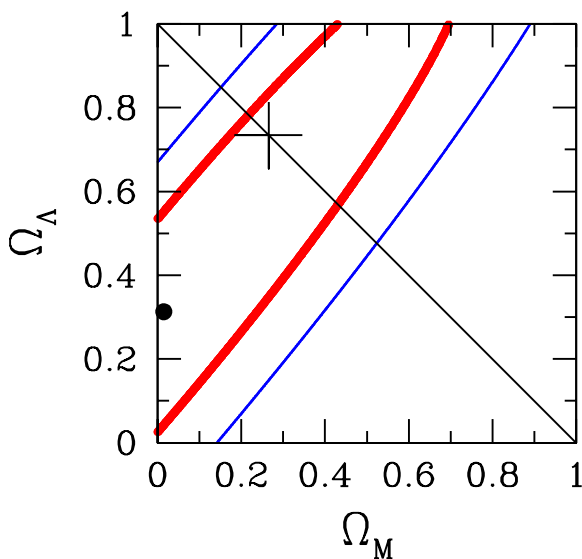


FIG. 14.— Constraints on Ω_M and Ω_Λ from fitting the angular diameter distances determined from isophotal sizes. The thick and thin contours mark the boundaries of the 1 and 2σ confidence regions, respectively. The circle denotes the best fit $\Omega_M = 0.02$, $\Omega_\Lambda = 0.31$, and the cross marks our adopted cosmology for this paper, $\Omega_M = 0.266$, $\Omega_\Lambda = 0.734$.

8. SCATTER IN SCALING RELATIONS

This paper has focused on the evolution of the normalization of observable-temperature scaling relations. Here we briefly discuss the *scatter* about those scaling relations, i.e., the variation in the ICM distribution from cluster to cluster at fixed temperature. Understanding the precise origins of scatter helps both in understanding cluster physics such as cool core development and merger effects, and in understanding sources of uncertainty in cosmological studies that use observables such as X-ray luminosity and temperature as proxies for cluster mass. As shown by O'Hara et al. (2006), the cluster central surface brightness I_0 is strongly correlated with central cooling time and reflects the core structure of clusters. In this section we examine the use of I_0 to reduce scatter in scaling relations, and to examine the redshift evolution of cluster structure.

8.1. Reducing Scatter: Two Approaches

As shown in previous sections, the total scatter in scaling relations generally decreases when core-subtracted quantities are used, reflecting the separation in cool core and non-cool core populations that is observed in most scaling relations (e.g., Fabian et al. 1994; Markevitch 1998; McCarthy et al. 2004; O'Hara et al. 2006). O'Hara et al. (2006) demonstrated that central surface brightness I_0 can be used as a proxy for cool core “strength” in a three parameter ($\mathcal{O}-T_X-I_0$) scaling relation, reducing the scatter in scaling relations that is introduced by biases to both the temperature and to the other observable (L_X , M_g , R_I) in the relation. With the data presented here we can compare the three-parameter approach to the use of core subtracted quantities, to determine whether either method results in lower scatter than the other.

Rather than using the β model values for I_0 , as in O'Hara et al. (2006), we estimate I_0 by simply averaging the surface brightness within $0.05r_{500}$ of the brightness peak. Since our intention is to use I_0 to parametrize the development of cool cores, this method is likely to give more accurate results than the surface brightness fitting which, even when a double β model is used, may not accurately reflect the structure around the brightness peak of a non-spherically symmetric cluster. We fit a scaling relation of the form

$$\mathcal{O} \propto T_X^\alpha I_0^\beta (1+z)^\gamma, \quad (13)$$

using the orthogonal fit (Eq. 11) appropriately modified for the additional parameter.

Table 5 gives the T_X dependence and intrinsic scatter for seven relations using non-core subtracted quantities (e.g., L_X-T_X), for the same relations using core subtracted quantities (e.g., $L_{\text{XCS}}-T_{\text{XCS}}$), and for the same relations adding the third parameter I_0 (e.g., $L_X-T_X-I_0$). The 3-parameter L_X relations have even lower intrinsic scatter than the core subtracted relations; for the M_g relations, the reverse is true. The scatter is little different between the different methods for the isophotal size relations, with perhaps slightly lower scatter in the core subtracted relations.

Interestingly, the slopes for the 3-parameter L_X relations are even lower than those of the core subtracted relations, and are $\sim 2\sigma$ lower than the self-similar expectation $\alpha = 2$. For the M_g and R_I relations, however,

TABLE 5
 SCATTER AND SLOPE COMPARISONS, CORE SUBTRACTED VS. 3-PARAMETER

Relation	Standard Relation		Core Subtracted		3-Parameter		
	α	σ_{int}	α	σ_{int}	α	β	σ_{int}
$L_{X,2500}-T_X$	$2.75^{+0.29}_{-0.26}$	$0.60^{+0.08}_{-0.09}$	$2.00^{+0.23}_{-0.19}$	0.28 ± 0.05	1.72 ± 0.13	0.39 ± 0.03	0.21 ± 0.03
$L_{X,500}-T_X$	$2.35^{+0.33}_{-0.24}$	$0.39^{+0.12}_{-0.10}$	$2.26^{+0.29}_{-0.33}$	$0.21^{+0.08}_{-0.07}$	1.72 ± 0.13	$0.28^{+0.06}_{-0.04}$	$0.15^{+0.02}_{-0.07}$
$M_{g,2500}-T_X$	1.82 ± 0.08	0.14 ± 0.02	$1.63^{+0.09}_{-0.08}$	$0.00^{+0.05}_{-0.00}$	1.70 ± 0.07	0.10 ± 0.02	0.07 ± 0.02
$M_{g,500}-T_X$	1.74 ± 0.09	0.13 ± 0.02	1.56 ± 0.10	0.09 ± 0.04	$1.70^{+0.10}_{-0.07}$	0.02 ± 0.02	0.12 ± 0.02
$R_{1.5 \times 10^{-13}}-T_X$	0.81 ± 0.07	0.13 ± 0.01	$0.70^{+0.07}_{-0.06}$	0.13 ± 0.02	0.89 ± 0.09	0.01 ± 0.02	0.13 ± 0.02
$R_{6 \times 10^{-14}}-T_X$	0.81 ± 0.09	0.16 ± 0.02	$0.66^{+0.09}_{-0.08}$	0.16 ± 0.02	0.82 ± 0.09	$-0.02^{+0.03}_{-0.02}$	0.16 ± 0.02
$R_{3 \times 10^{-14}}-T_X$	$0.74^{+0.08}_{-0.07}$	0.14 ± 0.02	0.65 ± 0.10	$0.12^{+0.03}_{-0.02}$	0.76 ± 0.08	-0.03 ± 0.02	0.13 ± 0.02

 NOTE. — Scatter is given in base e .

the 3-parameter slopes are consistent with those of the original relation, i.e., steeper than the core subtracted relations.

The M_g and R_I results by themselves would suggest that the three-parameter fit does not remove cool core-induced average temperature biases as completely as using core subtracted temperatures does; i.e., the brightness of a cluster's core is not a perfect indicator of the strength of the core. The reduced scatter in the three-parameter L_X relations compared with the core subtracted relations, however, indicates that differences in cool core and non-cool core clusters persist outside the $0.2r_{500}$ core exclusion radius. Together, these results may lend some additional weight to the argument that cool core and non-cool core clusters differ in ways other than their apparent relaxation as determined by the development of a cool, dense core.

to observational results that find a fairly constant cool core fraction of $\sim 50\%$ up to $z = 0.4$ (Bauer et al. 2005); O'Hara et al. (2006) showed that cool core-related effects, and not mergers, are the primary contributors to scaling relation scatter at low redshift, and so clearly accurate simulation of core evolution is required if simulations are to constrain the evolution of this scatter.

One way of gauging the effects of cool core development on scaling relation scatter is to look at the evolution of the central surface brightness I_0 . In Figure 15 we plot I_0 , measured as described in § 8.1, redshift. Like other cluster observables, I_0 should evolve with redshift as clusters grow and the average density drops with the cosmic expansion. Because I_0 is a measurement of the emission from a cluster along the line of sight through its center, i.e.,

$$I_0 \propto \int n_e^2 dr, \quad (14)$$

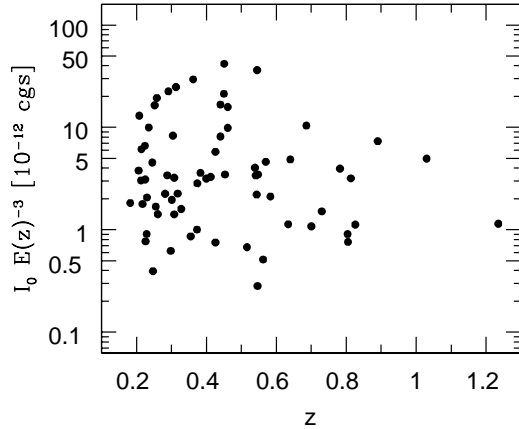


FIG. 15.— Central surface brightness I_0 versus redshift. The values of I_0 have been scaled by $E(z)^{-3}$, as described in the text, and are given in cgs units, i.e., $\text{erg s}^{-1} \text{cm}^{-2} \text{arcmin}^{-2}$.

8.2. Evolution of Scatter

As mentioned in § 4.2, we see a qualitative decrease in scatter at higher redshifts. Kay et al. (2007) found a decrease of a factor of ~ 3 in the luminosity–temperature relation in simulations, which they ascribe to merger effects at lower redshift. However, observational studies have found that clusters are in fact more structurally disturbed at higher redshift (e.g., Jeltema et al. 2005). Further more, cool cores are nearly ubiquitous in the Kay et al. (2007) simulations at all redshifts, in contrast

and density depends on redshift as $E(z)^2$, and cluster radius depends on redshift as $E(z)^{-1}$, we expect $I_0 \propto E(z)^3$ if clusters evolve self-similarly. Thus the values of I_0 in Figure 15 are scaled by $E(z)^{-3}$, and if clusters evolve self-similarly we would expect no average change with redshift in $I_0 E(z)^{-3}$ as plotted.

Qualitatively, however, it appears that the clusters with the highest I_0 appear at low redshift, indicating a change in core structure at these redshifts. This is consistent with our findings that scaling relations with core subtracted quantities evolve faster with redshift than those with non-core subtracted quantities. Furthermore, the overall scatter appears to increase at lower redshifts, consistent with what we have found in observable–temperature relations, indicating a wider range of core and other structural variations as clusters develop. Together, these trends can be explained by an increasing cool core fraction, or an increase the the strengths of cool cores in those clusters that have them, at lower redshifts. A larger sample of clusters would enable a more definitive investigation.

9. DISCUSSION

Our study indicates that cluster evolution is inconsistent with the simple self-similar model of cluster formation via gravitational collapse with no other heating or cooling processes. There is a substantial body of observational work in this area already, so in this section we discuss the similarities and differences between

our work and earlier studies of scaling relation evolution. The ultimate goal of such observations is to constrain models of cluster formation; predictions of how cluster evolution will be modified by non-gravitational processes can be made both via simple analytical models (e.g., Voit 2005) and from detailed hydrodynamical simulations (e.g., Muanwong et al. 2006).

9.1. Luminosity–Temperature

The X-ray luminosity–temperature relation is by far the most studied cluster scaling relation, with several studies using *Chandra* or XMM. These studies have generally found evolution in L_X – T_X relations that is either consistent with the self-similar expectation (e.g., Vikhlinin et al. 2002; Lumb et al. 2004; Kotov & Vikhlinin 2005; Maughan et al. 2006) or more negative (e.g., Ettori et al. 2004b; Branchesi et al. 2007). An interesting exception is Morandi et al. (2007), who found positive evolution when using their entire 24 cluster sample, but marginally negative evolution when using only the 11 clusters which were identified as having cool cores.

Qualitative examination of the redshift scaling in our sample (Figures 6, 9, and 12) clearly indicates the need to include clusters at redshifts as high as possible. Of the other studies mentioned above, the only ones that extend to redshifts beyond $z = 0.8$ are Ettori et al. (2004b) and Branchesi et al. (2007), who find negative evolution with respect to self-similar, as we do; Vikhlinin et al. (2002), who see no evolution with respect to self-similar, but whose methods (e.g., measurement of luminosities within fixed 2 Mpc apertures) are quite different from later studies, making comparison difficult; and Maughan et al. (2006), whose result is only marginally consistent with the self-similar expectation.

The work of Branchesi et al. (2007) in particular is interesting to compare to ours, because they use a *Chandra* sample covering a similar redshift range (though with only 17 members), and study two scenarios similar to our self-similar and no evolution scenarios. They find negative evolution with respect to self-similar, though at lower significance than our result; with an additional 22 clusters from three other *Chandra* studies, the significance increases. In a no evolution scenario, they find the L_X – T_X relation evolution to be consistent with zero, as we do in our $L_{X,2500}$ – T_X relation, which is most directly comparable. However, Branchesi et al. (2007) additionally measure scaling with respect to slopes and normalizations from local relations, obtain poor fits, and conclude that there is different evolution in the luminosity–temperature relation between $0 < z \lesssim 0.3$ and above this range. As discussed, however, there are systematic differences between cluster parameters measured with different instruments, or even the same instrument in different studies, as is shown in the Branchesi et al. (2007) results where fits worsen as additional clusters are added from other *Chandra* studies. If there is a sharp change at low redshift, quantifying it will require a homogeneously reduced sample, a task made unfortunately difficult for *Chandra* by its small field of view.

Results from simulations suggest possible explanations for the slower than self-similar evolution that we observe in the L_X – T_X relation. While not trying to exactly duplicate observed relations, Muanwong et al. (2006) produced simulations using different models for the in-

crease in entropy of the ICM. Their results show that, as naively expected, a simple radiative cooling model results in faster than self-similar evolution in luminosity–temperature because of reduced mean cluster temperatures and increased luminosities. They found slower than self-similar evolution using simple preheating and stellar feedback models, with the latter’s negative evolution significantly greater than the former. While their models are simple and cannot be directly used to test specific realistic models, these results do illustrate the usefulness of scaling relations in constraining cluster physics.

Ettori et al. (2004a) and Kay et al. (2007) have studied scaling relation evolution in simulations that include radiative cooling, star formation, and feedback. Both studies found significant ($\gg 3\sigma$) negative evolution with respect to self-similar in bolometric $L_{X,500}$ – T_X relations; specifically, Ettori et al. (2004a) found $\gamma = -0.76 \pm 0.08$ (depending on the exact method used; the other possible values are the same within the uncertainty), and Kay et al. (2007) found $\gamma = -0.98 \pm 0.03$ when using non-core subtracted quantities, and $\gamma = -0.61 \pm 0.04$ when measuring luminosities and temperatures excluding the central 50 kpc. Though direct comparisons may not be possible given differences in measurement of cluster temperatures between simulation and observation, differences in how the luminosities are measured, and the fact that our $L_{X,500}$ samples are relatively small and consequently have large uncertainties in their fit parameters, the simulation results are consistent with our results in Table 2 for $L_{X,500}$ and $L_{X,2500}$ relations. The more negative scaling in the non-core subtracted relation that Kay et al. (2007) found in simulations is matched by our data, and indicates that the primary source of the slower than self-similar evolution in the L_X – T_X relation is due to clusters being underluminous at higher redshifts, and not to temperature biases from cores. This slower than expected increase in luminosity at high redshifts indicates a potential source of difficulty for X-ray cosmology surveys, in that it may be more difficult to find large numbers of high-redshift clusters than has generally been assumed.

9.2. ICM Mass–Temperature

The ICM mass–temperature relation is less well studied than luminosity–temperature, and results are more varied. Vikhlinin et al. (2002) found significantly positive evolution relative to the self-similar expectation when measuring masses within a radius defined in terms of the average baryon density of the Universe; Ettori et al. (2004b) found marginally significant (1–2 σ) negative evolution with respect to self-similar ($\gamma = -(0.1-0.4)$, depending on the method used); Maughan et al. (2006) claim consistency of their high-redshift sample with low-redshift clusters when self-similar scaling is applied, though they do not attempt to directly measure any evolution; and Morandi et al. (2007) find significantly positive evolution with respect to self-similar. The simulations of Ettori et al. (2004a) predict negative evolution ($\gamma = -(0.1-0.2)$, depending on the method) at the 1–2 σ level. To this we compare our results, in which we find that M_g has negative evolution with respect to self-similar at the 1–3 σ level, depending on the radius and whether core subtracted parameters are used.

9.3. Gas Fraction

An unchanging gas mass fraction, or one that changes in easily quantifiable ways, is an essential component of cosmological studies that use measurements of cluster gas mass fractions to study cosmology (e.g., Rines et al. 1999; Ettori et al. 2003; Allen et al. 2004, 2007). There are, however, several complications to this use of f_g , which varies by cluster mass and by radius within a cluster (e.g., David et al. 1995; Mohr et al. 1999; Sanderson et al. 2003; Sadat et al. 2005). Sadat et al. (2005) claimed to find a decrease in f_g at higher redshifts when assuming a standard Λ CDM cosmology, consistent with our findings that f_g within r_{2500} decreases with redshift relative to the self-similar expectation. The angular diameter distance of clusters, which is used in these cosmological studies, varies with f_g as $d_A \propto f_g^{2/3}$, and so our observed $\sim 25\%$ decrease in f_g between redshifts 0 and 1 corresponds to a bias of $\sim 17\%$ in d_A estimates based on constant f_g over the same redshift range.

Simulations that include radiative cooling, star formation, and feedback processes likewise predict this decrease in f_g with redshift, with the magnitude of that decrease being larger at smaller fractions of the cluster virial radius (e.g., Kravtsov et al. 2005; Ettori et al. 2006). As with the L_X and M_g evolution, the predicted magnitude of this evolution differs according to the simulation parameters and the numerical codes used (Ettori et al. 2006), and so observational results such as ours will provide constraints as simulation quality improves.

As has been demonstrated Ferramacho & Blanchard (2007), the results obtained from cosmological studies that assume constant gas fraction depend heavily on the radius within which measurements are made, with radii closer to the virial radius giving results that disagree greatly with the concordance model. Though measurements at large radii require extrapolation that may introduce additional biases, such results when combined with evidence of the radial and redshift dependence of f_g give strong warning against ready acceptance of cosmological results that assume constant f_g , particularly when measurements are made at small radii such as r_{2500} .

Though our results suggest difficulties for cosmological studies that assume constant f_g , we have presented in §7.2 an alternative method for studying cosmology that involves using information about the evolution of f_g to measure angular diameter distances using isophotal sizes. This cosmic consistency test requires joint analysis of cluster structure, using L_X and M_g to constrain ICM evolution and R_I to estimate distances. Consistent input and output cosmological models are guaranteed only around the correct model.

10. CONCLUSIONS

We study the evolution of the ICM using X-ray scaling relations measured from a large, homogeneously analyzed sample of clusters spanning $0.2 \lesssim z \lesssim 1.2$. We use luminosity– and ICM mass–temperature relations, including both relations with and without core subtracted quantities, to test scenarios of standard “self-similar evolution” and of “no evolution”. We also study the evolution of isophotal size–temperature relations, for which (under certain assumptions) these two scenarios are identical. Finally, we compare the scatter in scaling relations after attempting to reduce cool core-induced scatter in two different ways. Our principal results appear below:

1. Luminosity– and ICM mass–temperature relations evolve less rapidly than expected in the self-similar evolution scenario; that is, clusters at higher redshifts have systematically lower luminosity and ICM mass at a given temperature than would be expected if clusters evolved self-similarly. The core subtracted relations have a combined consistency with the self-similar prediction of $< 0.1\%$; non-core subtracted relations are even more inconsistent with the self-similar prediction.
2. The data are also inconsistent with the no evolution scenario, though not at as strongly as in the self-similar scenario. The core subtracted relations evolve more rapidly than expected at higher redshift in this scenario, with combined probability of consistency with no evolution of 1%.
3. The evolution in the $L_{XCS}-T_{XCS}$ and M_g-T_{XCS} relations is consistent with a simple evolution in gas fraction, with evolution in f_g at $> 99\%$ confidence ($\gamma_{f_g} = -0.39 \pm 0.13$) in the self-similar evolution scenario when using core subtracted observables measured within r_{2500} .
4. Isophotal size evolves with redshift at a rate that depends on the isophote used, reflecting evolution in the ICM spatial distribution in clusters. Evolution of isophotal size at a low isophote (i.e., well away from the core) is consistent with that expected given the measured f_g evolution.
5. Relations with core subtracted quantities in general have more positive evolution than relations with the cores included, suggesting that either the cool core fraction decreases with increasing redshift, or that the cool core fraction remains constant but the cores that do exist are weaker at high redshift. This is supported by direct observations of the redshift dependence of central surface brightness, a good indicator of cool core development; the scatter and magnitude of I_0 increase at low redshift.
6. Core subtracted relations generally have temperature dependences that are shallower than non-core subtracted relations, and thus are more consistent with the slopes predicted by the self-similar model for each scaling relation.
7. The use of core subtracted quantities for scaling relations and the use of non-core subtracted quantities with the addition of a third parameter, the central surface brightness, both significantly reduce scaling relation scatter by compensating to some extent for cool core-related effects.
8. Scatter in observables at fixed temperature appears to decrease with redshift. This could indicate an increase in the cool core fraction, an increase in the strength of cool cores in those clusters that have them, or both.

Cluster simulations are still improving with regard to their ability to accurately model non-gravitational processes and thus to directly test specific models by comparison to observational data. However, our results of

negative evolution with respect to self-similar expectations in L_X and M_g , and consequently in f_g , provide important constraints for future computational studies. Our findings provide new warnings with regard to the assumptions made when using f_g measurements to study cosmology. It has long been established that f_g varies with radius inside clusters and varies with cluster mass when measured within r_{500} (e.g., David et al. 1993; Mohr et al. 1999). Our results strongly suggest that f_g varies with redshift as well. Given the differences in behavior of collisionless dark matter and the ICM (particularly the ICM's sensitivity to radiative cooling and feedback from AGN and supernovae), perhaps it should not be surprising that these components vary differentially with radius, cluster mass, and even redshift.

At the same time, the combination of isophotal size measurements with measurements of the evolution of f_g from L_X and M_g relations provides a promising tool for

measuring angular diameter distances. Our proposed cosmic consistency test would allow one to use cluster structure and its evolution to constrain cosmology in a manner complementary to more established techniques. Finally, our results underscore the need to directly calibrate (or self-calibrate) mass-observable scaling relations in large cluster survey cosmology experiments. Cluster structural evolution is subject to a wide range of interesting physics, and determining that mix reliably enough for even the most sophisticated simulations to precisely predict cluster mass-observable scaling relations and their evolution will remain enormously challenging for the foreseeable future.

This work was supported by the NASA Long Term Space Astrophysics award NAG 5-11415, NASA GSRP fellowship NNG05GO42H, and NSF Grant No. 0611808.

REFERENCES

- Allen, S. W., Rapetti, D. A., Schmidt, R. W., Ebeling, H., Morris, G., & Fabian, A. C. 2007, MNRAS, submitted (arXiv:0706.3277)
- Allen, S. W., Schmidt, R. W., Ebeling, H., Fabian, A. C., & van Speybroeck, L. 2004, MNRAS, 353, 457
- Arnaud, M., & Evrard, A. E. 1999, MNRAS, 305, 631
- Arnaud, M., Pointecouteau, E., & Pratt, G. W. 2005, A&A, 441, 893
- Balestra, I., Tozzi, P., Ettori, S., Rosati, P., Borgani, S., Mainieri, V., Norman, C., & Viola, M. 2007, A&A, 462, 429
- Bauer, F. E., Fabian, A. C., Sanders, J. S., Allen, S. W., & Johnstone, R. M. 2005, MNRAS, 359, 1481
- Bialek, J. J., Evrard, A. E., & Mohr, J. J. 2001, ApJ, 555, 597
- Borgani, S., Governato, F., Wadsley, J., Menci, N., Tozzi, P., Quinn, T., Stadel, J., & Lake, G. 2002, MNRAS, 336, 409
- Bower, R. G., Benson, A. J., Lacey, C. G., Baugh, C. M., Cole, S., & Frenk, C. S. 2001, MNRAS, 325, 497
- Branchesi, M., Gioia, I. M., Fanti, C., & Fanti, R. 2007, A&A, 472, 739
- Bryan, G. L. 2000, ApJ, 544, L1
- Burns, J. O., Hallman, E. J., Gantner, B., Motl, P. M., & Norman, M. L. 2007, ApJ, submitted (arXiv:0708.1954)
- Cash, W. 1979, ApJ, 228, 939
- Cavaliere, A., & Fusco-Femiano, R. 1978, A&A, 70, 677
- Cavaliere, A., Menci, N., & Tozzi, P. 1998, ApJ, 501, 493
- Crain, R. A., Eke, V. R., Frenk, C. S., Jenkins, A., McCarthy, I. G., Navarro, J. F., & Pearce, F. R. 2007, MNRAS, 377, 41
- David, L. P., Jones, C., & Forman, W. 1995, ApJ, 445, 578
- David, L. P., Slyz, A., Jones, C., Forman, W., Vrtilek, S. D., & Arnaud, K. A. 1993, ApJ, 412, 479
- de Propris, R., Stanford, S. A., Eisenhardt, P. R., Dickinson, M., & Elston, R. 1999, AJ, 118, 719
- Dickey, J. M., & Lockman, F. J. 1990, ARA&A, 28, 215
- Edge, A. C., & Stewart, G. C. 1991, MNRAS, 252, 414
- Eisenstein, D. J., Zehavi, I., Hogg, D. W., Scoccimarro, R., Blanton, M. R., Nichol, R. C., Scranton, R., Seo, H.-J., Tegmark, M., Zheng, Z., Anderson, S. F., Annis, J., Bahcall, N., Brinkmann, J., Burles, S., Castander, F. J., Connolly, A., Csabai, I., Doi, M., Fukugita, M., Frieman, J. A., Glazebrook, K., Gunn, J. E., Hendry, J. S., Hennessy, G., Ivezić, Z., Kent, S., Knapp, G. R., Lin, H., Loh, Y.-S., Lupton, R. H., Margon, B., McKay, T. A., Meiksin, A., Munn, J. A., Pope, A., Richmond, M. W., Schlegel, D., Schneider, D. P., Shimasaku, K., Stoughton, C., Strauss, M. A., SubbaRao, M., Szalay, A. S., Szapudi, I., Tucker, D. L., Yanny, B., & York, D. G. 2005, ApJ, 633, 560
- Ettori, S., Borgani, S., Moscardini, L., Murante, G., Tozzi, P., Diaferio, A., Dolag, K., Springel, V., Tormen, G., & Tornatore, L. 2004a, MNRAS, 354, 111
- Ettori, S., De Grandi, S., & Molendi, S. 2002, A&A, 391, 841
- Ettori, S., Dolag, K., Borgani, S., & Murante, G. 2006, MNRAS, 365, 1021
- Ettori, S., Tozzi, P., Borgani, S., & Rosati, P. 2004b, A&A, 417, 13
- Ettori, S., Tozzi, P., & Rosati, P. 2003, A&A, 398, 879
- Fabian, A. C., Crawford, C. S., Edge, A. C., & Mushotzky, R. F. 1994, MNRAS, 267, 779
- Ferramacho, L. D., & Blanchard, A. 2007, A&A, 463, 423
- Ferrari, C., Arnaud, M., Ettori, S., Maurogordato, S., & Rho, J. 2006, A&A, 446, 417
- Ferrari, C., Maurogordato, S., Cappi, A., & Benoist, C. 2003, A&A, 399, 813
- Ikebe, Y., Ezawa, H., Fukazawa, Y., Hirayama, M., Ishisaki, Y., Kikuchi, K., Kubo, H., Makishima, K., Matsushita, K., Ohashi, T., Takahashi, T., & Tamura, T. 1996, Nature, 379, 427
- Ikebe, Y., Makishima, K., Fukazawa, Y., Tamura, T., Xu, H., Ohashi, T., & Matsushita, K. 1999, ApJ, 525, 58
- Jee, M. J., White, R. L., Ford, H. C., Blakeslee, J. P., Illingworth, G. D., Coe, D. A., & Tran, K.-V. H. 2005, ApJ, 634, 813
- Jeltema, T. E., Canizares, C. R., Bautz, M. W., & Buote, D. A. 2005, ApJ, 624, 606
- Jones, C., & Forman, W. 1984, ApJ, 276, 38
- Kaiser, N. 1986, MNRAS, 222, 323
- Kay, S. T., da Silva, A. C., Aghanim, N., Blanchard, A., Liddle, A. R., Puget, J.-L., Sadat, R., & Thomas, P. A. 2007, MNRAS, 377, 317
- Kotov, O., & Vikhlinin, A. 2005, ApJ, 633, 781
- Kravtsov, A. V., Nagai, D., & Vikhlinin, A. A. 2005, ApJ, 625, 588
- Kravtsov, A. V., Vikhlinin, A., & Nagai, D. 2006, ApJ, 650, 128
- Lin, Y.-T., Mohr, J. J., Gonzalez, A. H., & Stanford, S. A. 2006, ApJ, 650, L99
- Lopes, P. A. A., de Carvalho, R. R., Capelato, H. V., Gal, R. R., Djorgovski, S. G., Brunner, R. J., Odewahn, S. C., & Mahabal, A. A. 2006, ApJ, 648, 209
- Lumb, D. H., Bartlett, J. G., Romer, A. K., Blanchard, A., Burke, D. J., Collins, C. A., Nichol, R. C., Giard, M., Marty, P. B., Nevalainen, J., Sadat, R., & Vaclair, S. C. 2004, A&A, 420, 853
- Markevitch, M. 1998, ApJ, 504, 27
- Maughan, B. J., Jones, C., Forman, W., & Van Speybroeck, L. 2007, ApJS, in press (astro-ph/0703156)
- Maughan, B. J., Jones, L. R., Ebeling, H., & Scharf, C. 2006, MNRAS, 365, 509
- McCarthy, I. G., Balogh, M. L., Babul, A., Poole, G. B., & Horner, D. J. 2004, ApJ, 613, 811
- Mohr, J. J., & Evrard, A. E. 1997, ApJ, 491, 38
- Mohr, J. J., Mathiesen, B., & Evrard, A. E. 1999, ApJ, 517, 627
- Mohr, J. J., Reese, E. D., Ellingson, E., Lewis, A. D., & Evrard, A. E. 2000, ApJ, 544, 109
- Morandi, A., Ettori, S., & Moscardini, L. 2007, MNRAS, 379, 518
- Muanwong, O., Kay, S. T., & Thomas, P. A. 2006, ApJ, 649, 640
- O'Hara, T. B., Mohr, J. J., Bialek, J. J., & Evrard, A. E. 2006, ApJ, 639, 64
- Ponman, T. J., Sanderson, A. J. R., & Finoguenov, A. 2003, MNRAS, 343, 331
- Pratt, G. W., Böhringer, H., Croston, J. H., Arnaud, M., Borgani, S., Finoguenov, A., & Temple, R. F. 2007, A&A, 461, 71

- Rines, K., Forman, W., Pen, U., Jones, C., & Burg, R. 1999, *ApJ*, 517, 70
- Sadat, R., Blanchard, A., Vauclair, S. C., Lumb, D. H., Bartlett, J., Romer, A. K., Bernard, J.-P., Boer, M., Marty, P., Nevalainen, J., Burke, D. J., Collins, C. A., & Nichol, R. C. 2005, *A&A*, 437, 31
- Sanderson, A. J. R., Finoguenov, A., & Mohr, J. J. 2005, *ApJ*, 630, 191
- Sanderson, A. J. R., Ponman, T. J., Finoguenov, A., Lloyd-Davies, E. J., & Markevitch, M. 2003, *MNRAS*, 340, 989
- Spiegel, D. N., Bean, R., Doré, O., Nolte, M. R., Bennett, C. L., Dunkley, J., Hinshaw, G., Jarosik, N., Komatsu, E., Page, L., Peiris, H. V., Verde, L., Halpern, M., Hill, R. S., Kogut, A., Limon, M., Meyer, S. S., Odegard, N., Tucker, G. S., Weiland, J. L., Wollack, E., & Wright, E. L. 2007, *ApJS*, 170, 377
- Vikhlinin, A., Burenin, R., Forman, W. R., Jones, C., Hornstrup, A., Murray, S. S., & Quintana, H. 2006, *Proc. Heating vs. Cooling in Galaxies and Clusters of Galaxies*, in press ([astro-ph/0611438](#))
- Vikhlinin, A., Markevitch, M., Murray, S. S., Jones, C., Forman, W., & Van Speybroeck, L. 2005, *ApJ*, 628, 655
- Vikhlinin, A., VanSpeybroeck, L., Markevitch, M., Forman, W. R., & Grego, L. 2002, *ApJ*, 578, L107
- Voit, G. M. 2005, *Rev. Mod. Phys.*, 77, 207
- Zhang, Y.-Y., Finoguenov, A., Böhringer, H., Kneib, J.-P., Smith, G. P., Czoske, O., & Soucail, G. 2007, *A&A*, 467, 437

TABLE 6
OBSERVATION AND SPECTRAL FITTING INFORMATION

Cluster	z	ObsID	$t_{\text{exp}}^{\text{a}}$ (ks)	RA ^b	DEC ^b	T_{X} aperture (arcsec)	T_{X} (keV)	T_{XCS} , SS ev. ^c (keV)	T_{XCS} , no ev. ^d (keV)
A665	0.182	3586	29.6	08:30:50.2	+65:52:14	380	8.0±0.2	8.1±0.3	8.2±0.3
A963	0.206	903	29.9	10:17:03.8	+39:02:42	195	7.0±0.3	6.8 ^{+0.4} _{-0.5}	6.8 ^{+0.4} _{-0.5}
RX J0439.0+0520...	0.208	527	9.6	04:39:02.3	+05:20:45	204	4.3 ^{+0.4} _{-0.3}	4.0 ^{+0.9} _{-0.6}	4.0 ^{+0.9} _{-0.6}
A1423	0.213	538	9.7	11:57:18.1	+33:36:45	256	6.0±0.4	6.2±0.7	6.3 ^{+0.8} _{-0.7}
ZwCl 2701	0.214	3195	18.3	09:52:49.3	+51:53:05	150	4.7±0.2	5.8±0.6	6.0 ^{+0.7} _{-0.6}
A773	0.217	5006	19.8	09:17:53.0	+51:43:37	257	8.3±0.4	8.0±0.6	8.1 ^{+0.7} _{-0.6}
A2261	0.224	5007	24.3	17:22:27.1	+32:07:56	275	7.7 ^{+0.3} _{-0.2}	7.3±0.5	7.1±0.5
ACO 2246	0.225	547	48.2	17:00:41.5	+64:12:53	103	2.9 ^{+0.3} _{-0.2}	1.8 ^{+0.3} _{-0.2}	1.7 ^{+0.3} _{-0.2}
A1682	0.226	3244	4.7	13:06:55.1	+46:33:01	254	5.5 ^{+0.8} _{-0.4}	5.4 ^{+1.0} _{-0.6}	5.6 ^{+1.1} _{-0.6}
A2111	0.229	544	10.2	15:39:39.6	+34:25:55	298	7.2±0.7	7.1 ^{+1.0} _{-0.9}	6.6 ^{+1.1} _{-0.6}
A267	0.230	3580	19.9	01:52:42.1	+01:00:33	254	7.1 ^{+0.4} _{-0.5}	6.8 ^{+1.1} _{-0.8}	7.1 ^{+0.9} _{-0.8}
RX J2129.7+0005...	0.235	552	9.9	21:29:40.1	+00:05:18	218	5.7±0.3	6.7 ^{+1.1} _{-0.6}	6.8 ^{+1.3} _{-0.6}
RX J0439.0+0715...	0.245	3583	19.2	04:39:00.8	+07:15:58	243	7.4±0.6	6.7 ^{+1.0} _{-0.7}	7.0 ^{+1.3} _{-1.0}
A521	0.247	901	38.1	04:54:08.1	-10:14:21	360	6.0±0.4	5.4 ^{+0.5} _{-0.3}	5.4 ^{+1.0} _{-0.3}
A1835	0.252	495	18.4	14:01:01.9	+02:52:41	187	8.2±0.2	16.3 ^{+3.3} _{-2.5}	16.1 ^{+3.6} _{-2.9}
A68	0.255	3250	9.9	00:37:06.4	+09:09:27	260	8.6 ^{+1.4} _{-0.8}	8.4 ^{+1.9} _{-1.6}	8.0 ^{+2.0} _{-1.6}
MS 1455.0+2232...	0.258	4192	91.6	14:57:15.1	+22:20:34	148	4.7±0.1	5.6±0.3	5.6±0.3
MS 1006.0+1202...	0.261	925	15.4	10:08:47.5	+11:47:34	234	6.1±0.4	6.6 ^{+1.1} _{-0.7}	6.6 ^{+1.4} _{-0.7}
A697	0.282	4217	19.5	08:42:57.6	+36:21:55	276	10.5 ^{+0.9} _{-0.5}	11.9±1.2	11.6±1.3
A611	0.288	3194	24.3	08:00:56.8	+36:03:23	172	8.9 ^{+0.7} _{-0.6}	11.8 ^{+3.6} _{-2.2}	12.5 ^{+3.3} _{-2.8}
ZwCl 3146	0.291	909	43.7	10:23:39.6	+04:11:10	246	6.5±0.1	8.7 ^{+0.7} _{-0.4}	8.6 ^{+0.7} _{-0.5}
A781	0.298	534	9.9	09:20:21.6	+30:30:20	264	5.3 ^{+0.6} _{-0.4}	5.3 ^{+0.7} _{-0.4}	5.2 ^{+0.6} _{-0.4}
MS 1008.1-1224...	0.301	926	28.6	10:10:32.2	-12:39:23	196	6.4±0.4	6.5 ^{+0.9} _{-0.6}	6.6 ^{+1.0} _{-0.6}
RXC J2245.0+2637	0.304	3287	14.6	22:45:04.9	+26:38:02	150	5.9±0.3	7.1 ^{+1.2} _{-0.9}	6.7 ^{+1.3} _{-0.8}
A1300	0.308	3276	13.7	11:31:55.3	-19:54:46	268	8.8 ^{+0.7} _{-0.6}	9.4 ^{+1.0} _{-0.9}	9.1 ^{+1.0} _{-0.9}
A2744	0.308	2212	22.1	00:14:15.3	-30:22:50	235	10.1±0.6	9.2 ^{+0.7} _{-0.6}	9.3±0.7
MS 2137.3-2353...	0.313	5250	25.6	21:40:15.2	-23:39:38	148	5.0±0.2	5.0±0.5	5.2 ^{+0.3} _{-0.6}
A1995	0.318	906	10.0	14:52:58.6	+58:02:58	191	8.1 ^{+1.0} _{-0.8}	6.0 ^{+1.0} _{-0.8}	5.7 ^{+1.1} _{-0.8}
ZwCl 1358+6245...	0.327	516	20.0	13:59:51.4	+62:30:53	185	9.1 ^{+0.9} _{-0.8}
A1722	0.328	3278	14.6	13:20:08.3	+70:04:34	203	9.1 ^{+1.5} _{-1.2}	13.2 ^{+6.4} _{-4.2}	10.6 ^{+7.4} _{-2.9}
RXC J0404.6+1109	0.355	3269	21.8	04:04:33.7	+11:08:25	321	5.6 ^{+0.8} _{-0.7}	5.1 ^{+0.9} _{-0.6}	5.1 ^{+1.0} _{-0.6}
RX J1532.9+3021...	0.362	1649	8.1	15:32:54.0	+30:21:04	128	6.1±0.3	8.1 ^{+1.6} _{-1.2}	7.5 ^{+1.6} _{-1.1}
A370	0.373	515	53.9	02:39:54.5	-01:34:47	184	8.7 ^{+0.5} _{-0.4}	8.1±0.5	7.8±0.5
ZwCl 1953	0.374	1959	21.0	08:50:08.4	+36:04:35	214	7.6±0.5	6.5 ^{+0.6} _{-0.5}	6.2±0.5
RXC J0949.8+1707	0.383	3274	14.3	09:49:52.4	+17:07:10	246	7.8 ^{+0.7} _{-0.6}	8.1 ^{+1.2} _{-1.1}	7.5±1.2
CIG J1416+4446...	0.400	541	29.9	14:16:28.4	+44:46:42	128	3.8±0.3	4.5 ^{+0.7} _{-0.5}	4.3 ^{+0.8} _{-0.5}
RXC J2228.6+2036	0.412	3285	19.8	22:28:32.1	+20:37:23	244	8.1±0.5	7.9 ^{+0.8} _{-0.7}	8.4 ^{+1.4} _{-0.8}
MS 0302.7+1658...	0.426	525	10.0	03:05:31.7	+17:10:05	82	3.6 ^{+0.5} _{-0.4}	2.8 ^{+0.7} _{-0.5}	2.7 ^{+0.5} _{-0.4}
MS 1621.5+2640...	0.426	546	30.0	16:23:35.0	+26:34:26	197	6.4 ^{+0.8} _{-0.5}	6.4 ^{+0.8} _{-0.7}	6.3 ^{+0.8} _{-0.7}
MACS J0417.5-1154	0.440	3270	11.9	04:17:33.5	-11:53:58	270	9.4±0.7	11.4 ^{+1.9} _{-1.6}	10.6 ^{+2.3} _{-1.3}
RXC J1206.2-0848...	0.440	3277	23.4	12:06:12.2	-08:48:05	236	11.4±0.9	12.5 ^{+1.7} _{-1.5}	12.7 ^{+2.1} _{-1.8}
CIG J0329-0212...	0.450	6108	39.5	03:29:41.6	-02:11:46	127	5.9±0.2	6.8 ^{+1.1} _{-0.6}	7.2 ^{+1.0} _{-0.8}
RX J1347.5-1145...	0.451	3592	57.7	13:47:30.7	-11:45:11	167	13.4 ^{+0.5} _{-0.3}	13.6 ^{+1.7} _{-0.9}	12.8 ^{+1.3} _{-0.8}
CIG J1701+6414...	0.453	547	48.2	17:01:24.0	+64:14:11	108	4.7±0.3	5.3 ^{+0.9} _{-0.5}	5.1 ^{+0.8} _{-0.6}
3C 295	0.461	2254	79.8	14:11:20.2	+52:12:08	128	5.7±0.2	5.4 ^{+0.6} _{-0.5}	5.1 ^{+0.7} _{-0.5}
CIG J1621+3810...	0.461	6172	29.8	16:21:25.0	+38:10:07	118	6.8 ^{+0.6} _{-0.4}	7.4 ^{+1.4} _{-1.3}	8.2 ^{+2.4} _{-1.7}
CIG J1524+0957...	0.516	1664	50.1	15:24:39.8	+09:57:46	112	4.8±0.4	4.6 ^{+0.6} _{-0.5}	4.9 ^{+0.7} _{-0.6}
MS 0451.6-0305...	0.539	902	32.3	04:54:11.9	-03:00:56	147	9.7±0.8	8.5 ^{+1.1} _{-0.8}	8.3 ^{+1.4} _{-1.0}
MS 0015.9+1609...	0.541	520	67.4	00:18:33.7	+16:26:17	197	9.7±0.5	9.9 ^{+0.7} _{-0.6}	10.1 ^{+0.9} _{-0.8}
CIG J1149+2223...	0.544	3589	20.0	11:49:35.7	+22:24:04	177	9.8±0.8	9.1 ^{+1.0} _{-0.9}	9.0 ^{+1.2} _{-0.9}
CIG J1423+2404...	0.545	4195	103.6	14:23:47.8	+24:04:41	156	5.4 ^{+0.2} _{-0.1}	5.0±0.3	4.6±0.3
CIG J1354-0221...	0.546	5835	37.5	13:54:17.2	-02:21:50	94	4.1 ^{+0.8} _{-0.3}	4.0 ^{+1.1} _{-0.9}	3.9 ^{+1.2} _{-1.0}
CIG J0717+3745...	0.548	4200	59.1	07:17:31.3	+37:45:35	244	11.5 ^{+0.7} _{-0.8}	10.3 ^{+0.8} _{-0.6}	9.9±0.6
CIG J1120+2326...	0.562	1660	69.3	11:20:57.5	+23:26:34	128	4.2 ^{+0.6} _{-0.3}	4.7±0.7	3.9±0.4
CIG J2129-0741...	0.570	3595	19.9	21:29:26.2	-07:41:28	166	11.8 ^{+2.8} _{-2.4}	9.0 ^{+2.7} _{-1.2}	8.9 ^{+3.5} _{-1.5}
MS 2053.7-0449...	0.583	1667	44.5	20:56:21.3	-04:37:49	69	4.0 ^{+0.5} _{-0.2}	3.6 ^{+0.8} _{-0.5}	3.2 ^{+0.8} _{-0.5}
CIG J0647+7015...	0.584	3584	19.9	06:47:50.6	+70:14:54	160	15.0 ^{+3.8} _{-2.7}
CIG J0542-4100...	0.634	914	48.6	05:42:49.6	-40:59:58	118	6.4 ^{+0.8} _{-0.7}	5.4 ^{+1.0} _{-0.6}	6.2 ^{+1.2} _{-1.0}
CIG J1419+5326...	0.640	3240	9.1	14:19:12.2	+53:26:09	59	4.1 ^{+0.8} _{-0.6}	3.4 ^{+0.8} _{-0.7}	3.1 ^{+0.8} _{-0.8}
CIG J0744+3927...	0.686	6111	49.5	07:44:52.8	+39:27:27	118	9.6±0.9	11.7 ^{+2.2} _{-2.0}	10.4 ^{+3.2} _{-2.1}
CIG J1221+4918...	0.700	1662	78.3	12:21:25.9	+49:18:28	138	6.5 ^{+0.8} _{-0.6}	6.4 ^{+1.0} _{-0.7}	6.1 ^{+0.9} _{-0.8}
CIG J1113-2615...	0.730	915	62.5	11:13:05.0	-26:15:40	79	3.7 ^{+0.6} _{-0.5}	2.8 ^{+0.6} _{-0.4}	2.6 ^{+0.6} _{-0.4}
CIG J137+6625...	0.782	536	27.6	11:40:22.4	+66:08:16	98	5.9 ^{+1.2} _{-0.9}	6.1 ^{+2.5} _{-1.7}	6.4 ^{+4.4} _{-2.2}
RX J1350.0+6007...	0.804	2229	58.3	13:50:48.3	+60:07:11	98	4.1 ^{+0.8} _{-0.6}	4.3 ^{+1.6} _{-0.8}	4.5 ^{+2.1} _{-1.2}
RX J1317+2911...	0.805	2228	111.3	13:17:21.8	+29:11:19	69	3.8 ^{+1.7} _{-0.9}	3.7 ^{+3.1} _{-1.1}	2.2 ^{+3.0} _{-0.6}
RX J1716+6708...	0.813	548	51.2	17:16:49.1	+67:08:24	108	6.4 ^{+0.9} _{-0.8}	5.6 ^{+1.2} _{-0.8}	6.4 ^{+2.3} _{-1.4}
CIG J1056-0337...	0.826	512	66.7	10:56:59.5	-03:37:34	118	9.2 ^{+1.5} _{-1.2}	8.7 ^{+1.8} _{-1.1}	8.6 ^{+2.3} _{-1.5}
CIG J1226+3332...	0.890	3180	31.6	12:26:58.0	+33:32:46	108	12.2 ^{+1.8} _{-1.7}	13.6 ^{+4.0} _{-3.2}	10.3 ^{+5.1} _{-3.1}
CIG J1415+3611...	1.030	4163	89.2	14:15:11.2	+36:12:03	79	6.8 ^{+1.0} _{-0.7}	6.2 ^{+1.8} _{-1.1}	6.0 ^{+1.5} _{-1.0}
CIG J1252-2927...	1.235	4198	162.5	12:52:54.4	-29:27:16	69	5.7 ^{+1.4} _{-1.0}	5.3 ^{+1.6} _{-1.0}	5.2 ^{+2.4} _{-1.3}

^a Exposure time after light curve filtering. ^b Coordinates given are center of spectral extraction aperture. ^c Core-subtracted temperature measured assuming self-similar evolution of r_{δ} . ^d Core-subtracted temperature measured assuming no evolution of r_{δ} .

TABLE 7
 β MODEL PARAMETERS

Cluster	Fit aperture (arcsec)	β	I_1 (erg s ⁻¹ cm ⁻² arcmin ⁻²)	$R_{c,1}$ (arcsec)	I_2 (erg s ⁻¹ cm ⁻² arcmin ⁻²)	$R_{c,2}$ (arcsec)
A665	394	0.62±0.01	1.9±0.0 E-12	65.6 ^{+1.4} _{-1.3}
A963	197	0.55±0.00	6.6±0.1 E-12	21.1 ^{+0.5} _{-0.4}
RX J0439.0+0520...	148	0.67 ^{+0.04} _{-0.02}	3.0 ^{+0.5} _{-0.4} E-12	28.0 ^{+3.7} _{-3.3}	5.4±0.4 E-11	5.4 ^{+0.5} _{-0.4}
A1423	187	0.46±0.01	7.2 ^{+0.6} _{-0.5} E-12	10.5±0.8
ZwCl 2701	153	0.58±0.01	1.5±0.0 E-11	12.3±0.3
A773	256	0.60±0.01	2.6±0.1 E-12	41.2 ^{+1.4} _{-1.5}
A2261	148	0.55 ^{+0.01} _{-0.00}	1.2±0.0 E-11	18.1 ^{+0.6} _{-0.5}
ACO 2246	148	0.52±0.01	3.7±0.3 E-12	9.0 ^{+0.8} _{-0.7}
A1682	177	0.56 ^{+0.06} _{-0.04}	1.0±0.1 E-12	49.2 ^{+9.7} _{-7.5}
A2111	295	0.58±0.02	1.2±0.1 E-12	48.7 ^{+3.1} _{-3.2}
A267	276	0.62±0.01	3.3±0.1 E-12	33.3±1.2
RX J2129.7+0005...	157	0.60±0.01	7.4±0.9 E-12	23.4 ^{+2.3} _{-2.0}	6.2 ^{+0.6} _{-0.3} E-11	4.1±0.4
RX J0439.0+0715...	256	0.61±0.01	6.0 ^{+0.2} _{-0.1} E-12	26.1 ^{+0.8} _{-1.1}
A521	295	0.75±0.00	5.5±0.2 E-13	122.0±2.4
A1835	167	0.73±0.01	5.7±0.2 E-12	44.8 ^{+1.2} _{-1.4}	1.1±0.0 E-10	8.9±0.2
A68	246	0.75 ^{+0.03} _{-0.02}	2.3±0.1 E-12	53.0 ^{+3.3} _{-3.0}
MS 1455.0+2232....	148	0.61±0.00	6.4±0.1 E-11	8.9±0.1
MS 1006.0+1202....	216	0.70±0.02	1.7±0.1 E-12	48.0 ^{+2.8} _{-2.5}
A697	256	0.64±0.01	3.7±0.1 E-12	46.6 ^{+1.6} _{-1.5}
A611	172	0.60±0.01	8.4±0.3 E-12	18.4±0.6
ZwCl 3146	246	0.68 ^{+0.01} _{-0.00}	1.6±0.1 E-11	23.8±0.6	1.2±0.0 E-10	5.4±0.1
A781	226	1.47 ^{+0.36} _{-0.24}	6.9±0.3 E-13	157.2 ^{+28.0} _{-21.2}
MS 1008.1-1224....	197	0.65±0.02	2.4±0.1 E-12	35.0±1.8
RXC J2245.0+2637..	148	0.66±0.02	8.5±0.8 E-12	21.3 ^{+2.2} _{-1.6}	4.1 ^{+0.6} _{-0.5} E-11	4.1 ^{+0.6} _{-0.5}
A1300	207	0.49±0.01	4.9 ^{+0.3} _{-0.2} E-12	22.1 ^{+1.2} _{-1.3}
A2744	406	1.10±0.04	1.8±0.0 E-12	112.5 ^{+4.3} _{-3.8}
MS 2137.3-2353....	138	0.64±0.01	3.9 ^{+1.2} _{-0.9} E-11	10.2±1.1	1.1±0.0 E-10	3.3 ^{+0.5} _{-0.6}
A1995	216	0.82±0.03	3.5±0.1 E-12	43.5 ^{+2.2} _{-2.1}
ZwCl 1358+6245....	157	0.66 ^{+0.03} _{-0.01}	2.8±0.2 E-12	31.4 ^{+2.4} _{-1.8}	4.0 ^{+0.2} _{-0.4} E-11	3.8 ^{+0.4} _{-0.2}
A1722	148	0.64 ^{+0.05} _{-0.03}	2.1 ^{+0.4} _{-0.6} E-12	30.7 ^{+7.9} _{-3.9}	2.9 ^{+1.2} _{-0.8} E-12	7.2 ^{+4.4} _{-2.5}
RXC J0404.6+1109..	128	0.46 ^{+0.04} _{-0.03}	1.0±0.1 E-12	28.6 ^{+5.9} _{-4.9}
RX J1532.9+3021....	118	0.61±0.01	1.1±0.0 E-10	7.8 ^{+0.2} _{-0.3}
A370	187	0.81±0.02	1.7±0.0 E-12	59.4 ^{+2.1} _{-2.0}
ZwCl 1953	246	0.65±0.01	4.5±0.2 E-12	30.9 ^{+1.3} _{-1.4}
RXC J0949.8+1707..	153	0.63±0.02	6.0±0.3 E-12	27.8 ^{+1.9} _{-1.8}
CIG J1416+4446....	148	0.58 ^{+0.03} _{-0.02}	3.0 ^{+0.5} _{-0.7} E-12	16.6 ^{+3.3} _{-2.4}	2.3 ^{+0.9} _{-0.6} E-11	1.9 ^{+0.8} _{-0.5}
RXC J2228.6+2036..	172	0.64±0.02	5.3±0.2 E-12	31.0 ^{+1.8} _{-1.7}
MS 0302.7+1658....	98	0.54±0.02	1.5 ^{+0.3} _{-0.2} E-11	6.9 ^{+1.2} _{-1.0}
MS 1621.5+2640....	197	0.67±0.03	1.3±0.1 E-12	41.6 ^{+3.6} _{-2.9}
MACS J0417.5-1154	192	0.65±0.02	4.4±0.3 E-12	48.4 ^{+2.8} _{-3.3}	1.1±0.1 E-10	5.2±0.3
RXC J1206.2-0848..	197	0.60±0.01	1.7±0.1 E-11	19.1 ^{+0.7} _{-0.6}
CIG J0329-0212....	118	0.52±0.00	1.2±0.1 E-10	3.8 ^{+0.1} _{-0.2}
RX J1347.5-1145....	189	0.65±0.00	4.5±0.2 E-11	16.7 ^{+0.4} _{-0.5}	3.9±0.1 E-10	3.7±0.1
CIG J1701+6414....	148	0.58±0.02	1.1 ^{+0.2} _{-0.1} E-12	29.4 ^{+3.1} _{-3.4}	2.9 ^{+0.5} _{-0.3} E-11	2.7±0.3
3C 295	118	0.63±0.01	9.3 ^{+1.7} _{-1.4} E-12	13.1 ^{+1.4} _{-1.3}	1.3±0.1 E-10	2.7 ^{+0.2} _{-0.1}
CIG J1621+3810....	108	0.60±0.02	7.6 ^{+2.0} _{-1.6} E-12	14.8 ^{+2.5} _{-2.0}	9.2 ^{+1.2} _{-1.0} E-11	2.5 ^{+0.4} _{-0.3}
CIG J1524+0957....	128	0.95 ^{+0.14} _{-0.10}	1.1±0.1 E-12	56.2 ^{+8.2} _{-6.6}
MS 0451.6-0305....	459	0.85±0.02	9.2±0.2 E-12	37.9±1.1
MS 0015.9+1609....	216	0.70±0.01	6.5±0.2 E-12	37.5 ^{+1.1} _{-1.0}
CIG J1149+2223....	295	0.65±0.02	4.3±0.2 E-12	40.9 ^{+2.5} _{-2.2}
CIG J1423+2404....	98	0.65±0.01	4.2±0.4 E-12	22.0 ^{+1.4} _{-1.0}	2.3±0.0 E-10	3.7±0.1
CIG J1354-0221....	157	0.76 ^{+0.12} _{-0.08}	8.3 ^{+1.0} _{-0.8} E-13	39.8 ^{+8.3} _{-6.6}
CIG J0717+3745....	187	0.82±0.02	4.7±0.1 E-12	65.6 ^{+2.5} _{-2.2}
CIG J1120+2326....	148	1.74 ^{+0.54} _{-0.31}	9.9 ^{+0.5} _{-0.4} E-13	88.4 ^{+18.5} _{-12.6}
CIG J2129-0741....	166	0.62 ^{+0.02} _{-0.01}	1.1±0.1 E-11	18.6±1.2
MS 2053.7-0449....	89	0.63 ^{+0.05} _{-0.04}	3.9 ^{+0.5} _{-0.4} E-12	15.6 ^{+2.5} _{-2.1}
CIG J0647+7015....	148	0.63±0.02	1.3±0.1 E-11	18.4 ^{+1.3} _{-1.2}
CIG J0542-4100....	112	0.58±0.03	2.9±0.2 E-12	22.5 ^{+2.7} _{-2.4}
CIG J1419+5326....	118	0.60±0.03	1.9 ^{+0.4} _{-0.3} E-11	7.3 ^{+1.2} _{-1.1}
CIG J0744+3927....	148	0.56±0.01	4.4±0.2 E-11	8.5±0.4
CIG J1221+4918....	157	0.73 ^{+0.04} _{-0.03}	2.5±0.1 E-12	35.7 ^{+2.8} _{-2.6}
CIG J1113-2615....	98	0.73 ^{+0.08} _{-0.06}	4.3±0.5 E-12	15.8 ^{+2.8} _{-2.5}
CIG 1137+6625....	98	0.65 ^{+0.04} _{-0.03}	1.5 ^{+0.2} _{-0.1} E-11	12.4 ^{+1.4} _{-1.3}
RX J1350.0+6007....	148	0.61 ^{+0.05} _{-0.04}	2.3±0.3 E-12	21.4 ^{+3.9} _{-3.1}
RX J1317+2911....	89	0.84 ^{+0.40} _{-0.20}	5.3 ^{+1.9} _{-1.2} E-13	29.4 ^{+13.8} _{-9.8}	4.8 ^{+2.1} _{-1.2} E-12	4.3 ^{+2.4} _{-1.6}
RX J1716+6708....	148	0.68 ^{+0.04} _{-0.03}	8.3±0.6 E-12	17.3 ^{+1.9} _{-1.7}
CIG J1056-0337....	197	0.67±0.00	5.8±0.3 E-12	31.9±0.9
CIG J1226+3332....	128	0.68±0.02	3.3±0.2 E-11	14.5±1.0
CIG J1415+3611....	98	0.75 ^{+0.06} _{-0.04}	9.5±1.2 E-12	18.1±2.4	6.5 ^{+2.0} _{-1.4} E-11	2.5 ^{+0.6} _{-0.5}
CIG J1252-2927....	89	0.54±0.03	1.1±0.2 E-11	8.8 ^{+1.6} _{-1.4}

TABLE 8
CLUSTER MEASUREMENTS ASSUMING SELF-SIMILAR EVOLUTION

Cluster	$L_{X,2500}$ ($10^{44} L_{\odot}$)	$L_{X,500}$ ($10^{44} L_{\odot}$)	$M_{g,2500}$ ($10^{13} M_{\odot}$)	$M_{g,500}$ ($10^{13} M_{\odot}$)	$R_{1.5E-13}$ (Mpc)	R_{6E-14} (Mpc)	R_{3E-14} (Mpc)
A665.....	3.27±0.03	...	3.93±0.09	13.05±0.30	0.40±0.02
A963.....	2.95±0.03	...	2.86±0.08	9.27±0.27	0.33±0.02
RX J0439.0+0520..	2.17±0.02	...	1.42±0.07	3.79±0.19	0.23±0.01	0.31±0.02	0.40±0.04
A1423.....	1.98±0.04	...	2.08±0.07	8.01±0.28	0.28±0.01	0.46±0.04	...
ZwCl 2701.....	2.10±0.01	...	1.58±0.07	4.63±0.21	0.24±0.01	0.34±0.02	...
A773.....	2.92±0.03	...	3.55±0.09	11.34±0.30	0.36±0.02
A2261.....	4.69±0.03	...	3.81±0.11	12.20±0.36	0.38±0.02
ACO 2246.....	0.46±0.01	...	0.56±0.04	1.91±0.15	...	0.21±0.01	...
A1682.....	1.61±0.09	...	2.01±0.08	7.55±0.31	0.32±0.02	0.52±0.05	...
A2111.....	1.77±0.05	...	2.59±0.08	9.03±0.29	0.31±0.01	0.49±0.03	0.66±0.06
A267.....	2.37±0.03	...	2.73±0.09	8.15±0.27	0.30±0.01	0.43±0.03	0.57±0.05
RX J2129.7+0005..	4.26±0.03	...	2.75±0.11	8.13±0.33	0.34±0.02	0.49±0.04	0.63±0.07
RX J0439.0+0715..	3.28±0.04	...	3.20±0.11	9.43±0.31	0.35±0.02	0.49±0.03	0.61±0.05
A521.....	2.00±0.07	3.43±0.07	2.38±0.10	10.80±0.44	0.43±0.03	0.68±0.08	0.82±0.11
A1835.....	10.50±0.05	...	5.35±0.16	13.56±0.42	0.44±0.02
A68.....	2.84±0.07	...	3.68±0.11	9.96±0.29	0.35±0.01	0.48±0.03	...
MS 1455.0+2232...	4.95±0.01	5.45±0.04	2.20±0.12	6.05±0.33	0.30±0.02	0.41±0.04	...
MS 1006.0+1202...	1.85±0.03	...	2.37±0.10	7.21±0.31	0.29±0.01	0.41±0.03	...
A697.....	5.32±0.09	...	5.96±0.16	18.56±0.50	0.51±0.02	0.71±0.05	0.88±0.07
A611.....	2.91±0.03	...	3.29±0.11	9.50±0.31	0.32±0.01	0.44±0.02	...
ZwCl 3146.....	9.16±0.02	...	4.19±0.19	10.77±0.48	0.41±0.03	0.56±0.05	...
A781.....	1.43±0.09	...	2.05±0.12	7.99±0.45	0.37±0.03	0.59±0.07	0.74±0.10
MS 1008.1-1224....	1.93±0.03	...	2.44±0.11	7.44±0.35	0.33±0.02	0.45±0.03	0.56±0.05
RXC J2245.0+2637	3.47±0.02	3.85±0.05	2.54±0.13	6.82±0.35	0.30±0.02	0.41±0.03	0.51±0.04
A1300.....	4.04±0.09	5.55±0.11	4.28±0.15	15.90±0.56	0.46±0.02	0.69±0.05	...
A2744.....	4.74±0.10	...	6.10±0.19	17.12±0.52	0.58±0.03
MS 2137.3-2353....	5.15±0.02	...	2.27±0.14	5.87±0.37	0.29±0.02	0.39±0.03	0.49±0.05
A1995.....	2.88±0.04	...	3.45±0.14	8.43±0.33	0.34±0.01	0.44±0.02	0.56±0.04
ZwCl 1358+6245...	2.64±0.04	...	3.28±0.12	9.21±0.33	0.31±0.01	0.43±0.02	0.54±0.03
A1722.....	1.80±0.05	...	2.90±0.10	8.53±0.31	0.28±0.01	0.40±0.02	0.54±0.03
RXC J0404.6+1109	1.20±0.08	2.30±0.14	1.73±0.11	7.61±0.48	0.28±0.01	0.64±0.07	...
RX J1532.9+3021..	8.84±0.03	...	3.62±0.22	9.81±0.59	0.36±0.02	0.50±0.04	0.64±0.07
A370.....	2.59±0.05	...	3.84±0.16	11.46±0.49	0.40±0.02
ZwCl 1953.....	3.43±0.06	4.31±0.09	3.68±0.18	11.27±0.56	0.39±0.02	0.56±0.04	0.71±0.07
RXC J0949.8+1707	4.08±0.07	5.11±0.09	4.05±0.20	12.40±0.61	0.41±0.02	0.57±0.04	0.76±0.07
CIG J1416+4446...	1.10±0.02	1.44±0.05	1.14±0.12	3.78±0.40	0.24±0.01	0.34±0.03	0.44±0.05
RXC J2228.6+2036	4.15±0.08	5.66±0.08	4.43±0.23	13.92±0.71	0.50±0.03	0.69±0.06	0.82±0.08
MS 0302.7+1658...	1.41±0.02	...	1.15±0.14	3.76±0.45	0.23±0.01	0.33±0.03	0.43±0.05
MS 1621.5+2640...	1.41±0.05	2.09±0.09	2.15±0.14	7.60±0.51	0.32±0.02	0.48±0.04	0.70±0.08
MACS J0417.5-1154	10.27±0.19	13.17±0.11	7.14±0.33	24.15±1.13	0.63±0.04	0.82±0.07	0.97±0.10
RXC J1206.2-0848..	8.02±0.10	9.47±0.11	7.24±0.28	21.76±0.84	0.54±0.03	0.73±0.05	0.92±0.07
CIG J0329-0212....	5.23±0.03	5.92±0.09	2.89±0.22	9.37±0.72	0.37±0.02	0.52±0.05	0.65±0.07
RX J1347.5-1145...	18.85±0.05	...	10.10±0.34	25.94±0.87	0.56±0.02
CIG J1701+6414...	1.22±0.03	...	1.41±0.14	5.16±0.50	0.26±0.01	0.38±0.03	0.50±0.05
3C 295.....	2.91±0.01	...	2.06±0.17	5.62±0.45	0.27±0.01	0.36±0.02	0.46±0.04
CIG J1621+3810...	3.09±0.03	...	2.68±0.18	7.99±0.54	0.31±0.01	0.46±0.03	0.59±0.05
CIG J1524+0957...	0.92±0.04	1.47±0.08	1.47±0.16	5.28±0.57	0.29±0.02	0.43±0.04	0.52±0.06
MS 0451.6-0305....	6.09±0.09	7.06±0.16	6.18±0.34	15.86±0.88	0.48±0.02	0.62±0.04	...
MS 0015.9+1609...	5.76±0.08	7.61±0.11	6.14±0.34	19.43±1.08	0.55±0.03
CIG J1149+2223...	4.78±0.14	7.07±0.14	5.66±0.32	20.17±1.12	0.56±0.03	0.86±0.08	1.08±0.12
CIG J1423+2404...	5.54±0.02	6.23±0.10	2.75±0.28	7.91±0.80	0.34±0.02	0.49±0.05	...
CIG J1354-0221....	0.53±0.03	...	0.94±0.13	3.58±0.48	0.20±0.01	0.33±0.03	0.44±0.05
CIG J0717+3745...	7.78±0.23	11.13±0.13	8.51±0.41	29.57±1.41	0.68±0.04	0.88±0.07	...
CIG J1120+2326...	0.78±0.05	...	1.22±0.16	4.41±0.58	0.26±0.02	0.37±0.03	0.43±0.04
CIG J2129-0741....	4.22±0.17	...	5.56±0.27	16.45±0.80	0.42±0.01	0.63±0.03	0.80±0.05
MS 2053.7-0449....	0.89±0.02	...	1.13±0.17	3.58±0.52	0.23±0.01	0.33±0.03	0.40±0.04
CIG J0647+7015...	5.02±0.13	...	7.15±0.28	20.11±0.78	0.43±0.01	0.59±0.02	...
CIG J0542-4100....	1.33±0.05	1.95±0.08	2.08±0.21	7.58±0.75	0.34±0.02	0.47±0.03	0.58±0.05
CIG J1419+5326...	1.40±0.04	...	1.28±0.20	3.78±0.59	0.23±0.01	0.33±0.03	0.43±0.05
CIG J0744+3927...	5.49±0.09	...	5.03±0.36	15.80±1.13	0.47±0.02	0.64±0.04	0.79±0.06
CIG J1221+4918...	1.47±0.06	2.18±0.07	2.27±0.24	8.27±0.89	0.37±0.02	0.55±0.05	...
CIG J1113-2615....	0.64±0.02	...	0.91±0.18	2.64±0.52	0.20±0.01	0.27±0.02	0.35±0.03
CIG J137+6625....	1.88±0.07	...	2.12±0.28	6.17±0.82	0.29±0.01	0.41±0.03	0.53±0.05
RX J1350.0+6007..	0.60±0.05	1.04±0.05	1.01±0.20	4.05±0.80	0.26±0.02	0.41±0.04	0.53±0.07
RX J1317+2911....	0.20±0.02	...	0.52±0.11	1.77±0.38	...	0.21±0.01	0.32±0.03
RX J1716+6708....	1.64±0.05	...	2.25±0.29	6.77±0.86	0.31±0.02	0.43±0.03	0.54±0.05
CIG J1056-0337....	3.23±0.23	...	4.53±0.41	16.57±1.49	0.51±0.03	0.62±0.04	0.72±0.06
CIG J1226+3332....	4.80±0.11	...	5.94±0.44	15.86±1.16	0.44±0.02	0.59±0.03	0.71±0.04
CIG J1415+3611...	1.48±0.03	...	2.20±0.33	6.33±0.96	0.29±0.01	0.40±0.02	0.50±0.04
CIG J1252-2927....	0.63±0.04	...	1.28±0.28	4.63±1.01	0.28±0.01	0.42±0.03	0.54±0.05

TABLE 9
CLUSTER MEASUREMENTS ASSUMING NO EVOLUTION

Cluster	$L_{X,2500}$ ($10^{44} L_{\odot}$)	$M_{g,2500}$ ($10^{13} M_{\odot}$)	$M_{g,500}$ ($10^{13} M_{\odot}$)
A665.....	3.78±0.04	4.13±0.09	13.42±0.31
A963.....	...	2.99±0.09	9.63±0.28
RX J0439.0+0520..	2.45±0.03	1.46±0.07	3.84±0.19
A1423.....	2.33±0.05	2.22±0.08	8.53±0.30
ZwCl 2701.....	2.38±0.02	1.64±0.07	4.76±0.21
A773.....	3.40±0.04	3.74±0.10	11.72±0.31
A2261.....	5.41±0.03	3.99±0.12	12.70±0.37
ACO 2246.....	...	0.59±0.05	2.01±0.16
A1682.....	1.95±0.08	2.17±0.09	7.94±0.33
A2111.....	2.11±0.06	2.78±0.09	9.43±0.30
A267.....	2.75±0.03	2.86±0.09	8.38±0.27
RX J2129.7+0005..	4.91±0.03	2.87±0.12	8.37±0.34
RX J0439.0+0715..	3.83±0.04	3.35±0.11	9.71±0.32
A521.....	2.58±0.09	2.71±0.11	11.42±0.47
A1835.....	12.13±0.06	5.50±0.17	13.62±0.42
A68.....	3.33±0.06	3.85±0.11	10.04±0.30
MS 1455.0+2232...	5.74±0.01	2.27±0.13	6.20±0.34
MS 1006.0+1202...	2.23±0.04	2.52±0.11	7.38±0.31
A697.....	6.48±0.08	6.38±0.17	19.24±0.52
A611.....	3.46±0.05	3.45±0.11	9.84±0.32
ZwCl 3146.....	10.85±0.02	4.32±0.19	10.88±0.49
A781.....	1.97±0.11	2.39±0.13	8.03±0.45
MS 1008.1-1224....	2.41±0.04	2.61±0.12	7.69±0.36
RXC J2245.0+2637	4.16±0.03	2.65±0.14	6.94±0.36
A1300.....	5.09±0.09	4.71±0.16	17.25±0.60
A2744.....	...	6.67±0.20	16.77±0.51
MS 2137.3-2353....	6.15±0.03	2.33±0.15	5.98±0.37
A1995.....	3.51±0.05	3.59±0.14	8.33±0.33
ZwCl 1358+6245...	3.25±0.05	3.47±0.12	9.46±0.34
A1722.....	2.22±0.05	3.10±0.11	8.84±0.32
RXC J0404.6+1109	1.69±0.11	2.01±0.13	8.59±0.54
RX J1532.9+3021..	10.90±0.04	3.78±0.23	10.15±0.61
A370.....	3.49±0.07	4.25±0.18	11.62±0.50
ZwCl 1953.....	4.48±0.06	4.02±0.20	11.78±0.58
RXC J0949.8+1707	5.30±0.08	4.42±0.22	13.00±0.63
ClG J1416+4446...	1.48±0.03	1.27±0.13	4.06±0.43
RXC J2228.6+2036	5.71±0.11	4.92±0.25	14.68±0.75
MS 0302.7+1658...	...	1.27±0.15	4.09±0.49
MS 1621.5+2640...	1.98±0.06	2.50±0.17	8.13±0.54
MACS J0417.5-1154	14.27±0.22	8.17±0.38	25.86±1.21
RXC J1206.2-0848..	10.79±0.12	7.91±0.30	23.15±0.89
ClG J0329-0212....	6.94±0.04	3.19±0.24	10.32±0.79
RX J1347.5-1145...	24.62±0.06	10.58±0.35	26.60±0.89
ClG J1701+6414...	1.71±0.03	1.64±0.16	5.69±0.55
3C 295.....	3.86±0.02	2.19±0.18	5.85±0.47
ClG J1621+3810...	4.17±0.04	2.92±0.20	8.52±0.58
ClG J1524+0957...	1.48±0.05	1.83±0.20	5.43±0.59
MS 0451.6-0305....	8.82±0.11	6.74±0.37	15.49±0.86
MS 0015.9+1609...	8.78±0.10	7.14±0.40	20.52±1.15
ClG J1149+2223...	7.55±0.18	6.86±0.38	22.15±1.23
ClG J1423+2404...	7.87±0.05	3.03±0.31	8.36±0.84
ClG J1354-0221....	0.85±0.05	1.19±0.16	3.87±0.52
ClG J0717+3745...	12.73±0.23	10.46±0.50	31.03±1.48
ClG J1120+2326...	1.35±0.05	1.60±0.21	4.17±0.55
ClG J2129-0741....	6.34±0.21	6.23±0.30	17.66±0.86
MS 2053.7-0449....	1.37±0.03	1.31±0.19	3.88±0.57
ClG J0647+7015...	7.34±0.16	7.89±0.31	21.30±0.83
ClG J0542-4100....	2.29±0.08	2.59±0.26	8.68±0.86
ClG J1419+5326...	2.13±0.05	1.44±0.23	4.12±0.65
ClG J0744+3927...	8.90±0.13	5.86±0.42	18.02±1.29
ClG J1221+4918...	2.69±0.07	2.97±0.32	9.09±0.97
ClG J1113-2615....	1.02±0.04	1.06±0.21	2.73±0.54
ClG J1137+6625....	3.23±0.10	2.46±0.33	6.65±0.89
RX J1350.0+6007..	1.31±0.07	1.41±0.28	4.90±0.97
RX J1317+2911....	0.38±0.04	0.68±0.15	1.87±0.40
RX J1716+6708....	2.96±0.08	2.70±0.34	7.26±0.92
ClG J1056-0337....	6.67±0.16	6.14±0.55	19.02±1.71
ClG J1226+3332...	8.67±0.17	6.71±0.49	16.52±1.21
ClG J1415+3611...	3.03±0.08	2.68±0.41	6.53±0.99
ClG J1252-2927....	...	1.90±0.41	6.25±1.36